Exploring Sentinel-1 backscatter time series over the Atacama Desert (Chile) for seasonal dynamics of surface soil moisture

Tobias Ullmann, Thomas Jagdhuber, Dirk Hoffmeister, Simon Matthias May, Roland Baumhauer, Olaf Bubenzer

Angaben zur Veröffentlichung / Publication details:

Ullmann, Tobias, Thomas Jagdhuber, Dirk Hoffmeister, Simon Matthias May, Roland Baumhauer, and Olaf Bubenzer. 2023. "Exploring Sentinel-1 backscatter time series over the Atacama Desert (Chile) for seasonal dynamics of surface soil moisture." *Remote Sensing of Environment* 285: 113413. https://doi.org/10.1016/j.rse.2022.113413.

Remote Sensing of Environment 285 (2023) 113413

Contents lists available at ScienceDirect

Remote Sensing of Environment

journal homepage: www.elsevier.com/locate/rse

Exploring Sentinel-1 backscatter time series over the Atacama Desert (Chile) for seasonal dynamics of surface soil moisture

Tobias Ullmann [a,b,*], Thomas Jagdhuber [c,d], Dirk Hoffmeister [e], Simon Matthias May [e], Roland Baumhauer [a], Olaf Bubenzer [f]

[a] University of Würzburg, Institute of Geography and Geology, Physical Geography, Am Hubland, D-97074 Wuerzburg, Germany
[b] University of Würzburg, Institute of Geography and Geology, Department of Remote Sensing, Oswald Kuelpe Weg 86, D-97074 Wuerzburg, Germany
[c] German Aerospace Center (DLR), Microwaves and Radar Institute, Oberpfaffenhofen, 82234 Weßling, Germany
[d] University of Augsburg, Institute of Geography, 86159 Augsburg, Germany
[e] University of Cologne, Institute of Geography, Zülpicher Straße 45, D-50674 Köln, Germany
[f] University Heidelberg, Institute of Geography and Heidelberg Center for the Environment, Im Neuenheimer Feld 348, D-69120 Heidelberg, Germany,

ARTICLE INFO

Edited by Jing M. Chen

Keywords:
SAR
Sentinel-1
Intensity
Desert
Soil moisture
Subsurface scattering
Inversion
Anticorrelation

ABSTRACT

Recent research indicates an inverse relation between Synthetic Aperture Radar (SAR) signal and near-surface soil moisture (SM) over very dry sediments, arid to hyper-arid soils resp., caused by subsurface scattering effects. This phenomenon can lead to large errors when it comes to modelling and remote sensing-based estimation of SM. While the effect of subsurface scattering and its influence on SM estimates is well described and modelled in literature, its actual presence in recorded SAR data is largely unknown. Here we investigate the relation between C-Band SAR backscatter and SM in the hyper-arid environment of the Atacama Desert (Chile). Time series (2018–2020) of Sentinel-1 VV/VH intensities are compared to in situ SM, measured at 17 stations located across the Atacama Desert. Linear and non-linear regression modelling is applied to uncover the relationship between the SAR intensities and in situ SM, while, in addition, SM variations triggered by seasonal varying humidity (i.e., not by precipitation) are investigated. Results indicate (i) a very weak linear relationship between SM variations and SAR intensities (VV/VH) for most meteorological stations in the Atacama ($R^2 < 0.5$). In particular, noticeable and significant exceptions are found for stations located in the northern uplands of the Coastal Cordillera and on sediments, which are characterized by thick atmospheric dust deposits on top of subsurface cemented crusts; (ii) over these sites a strong inverse linear relationship is present (R^2 up to 0.84) and the observable seasonal variations in SAR intensity are linked to the seasonal variations in SM; (iii) remarkably low changes in SM (ranging from approx. 1 to 3%) lead to comparable high changes in SAR intensity (up to 5.5 dB in VH and up to 4.0 dB in VV); (iv) employing a non-linear regression modelling to the SAR time series allowed identifying the occurrence and the strength of seasonal variations over the central desert. This study contributes to a better understanding of SAR scattering over arid to hyper-arid soils, indicates a moisture-regulated complex interplay of surface and subsurface scattering, and proves the presence of subsurface scattering effects in Sentinel-1C-Band data to occur over large parts of the Atacama Desert.

1. Introduction

Soil moisture, defined as the water content in the topmost soil layer, is an important variable in the Earth's system and regulates feedbacks between the land and the atmosphere (Seneviratne et al., 2010; Yang et al., 2018). It is identified as an essential climate variable as it influences energy fluxes on land (latent and sensible heat), separates precipitation (runoff and infiltration), and determines the presence and condition of vegetation (mutually influenced by evapotranspiration) (Bojinski et al., 2014; Dorigo et al., 2017; Seneviratne et al., 2010). Thereby, soil moisture is highly heterogenous in space and in time and strongly influenced by meteorological, short-term climatic variations,

* Corresponding author at: University of Würzburg, Institute of Geography and Geology, Deparment of Remote Sensing, Oswald Kuelpe Weg 86, D-97074 Wuerzburg, Germany.
E-mail addresses: tobias.ullmann@uni-wuerzburg.de (T. Ullmann), thomas.jagdhuber@dlr.de (T. Jagdhuber), dirk.hoffmeister@uni-koeln.de (D. Hoffmeister), mays@uni-koeln.de (S.M. May), baumhauer@uni-wuerzburg.de (R. Baumhauer), olaf.bubenzer@uni-heidelberg.de (O. Bubenzer).

https://doi.org/10.1016/j.rse.2022.113413
Received 8 March 2022; Received in revised form 1 December 2022; Accepted 6 December 2022
Available online 21 December 2022

and/or pedologic conditions. From a geomorphological point of view, soil moisture influences several morphodynamic processes, such as mass wasting, physical and chemical weathering, and it is therefore an important factor altering and controlling pedogenesis, crust-formation, erosion and/or accumulation, especially on long timescales (Fryberger and Goudie, 1981; Legates et al., 2011). However, continuous, and area-wide estimation of soil moisture on ground is laborious and time consuming, even for measuring only the water content of the topmost soil layer. Therefore, in situ measurements are usually sparse and only available at selected locations (Montzka et al., 2021).

Accordingly, there are many efforts to estimate soil moisture using space-borne earth observation data (Wang and Qu, 2009), also including data of active/passive microwave sensors such as ASCAT (Wagner et al., 2013), ESA-CCI (Dorigo et al., 2017), SMOS (Kerr et al., 2012), SMAP (Chan et al., 2016; Colliander et al., 2017; Suman et al., 2020), Sentinel-1 (Balenzano et al., 2021; Bauer-Marschallinger et al., 2019), or combinations (Das et al., 2019; Montzka et al., 2016). In this context, the high applicability of active and passive systems, operating in the range of microwave radiation (approx. 1 to 300 GHz), has been extensively demonstrated in previous studies (Barrett et al., 2009; Jagdhuber et al., 2015; Kornelsen and Coulibaly, 2013; Li et al., 2021; Wagner et al., 2007). Thereby, the estimation of soil moisture via microwaves takes use of the relation between the soil moisture content and the dielectric properties of the target (Richards, 2009; Ulaby and Long, 2014). Active systems from Synthetic Aperture Radar (SAR) usually provide a higher spatial resolution compared to passive systems (microwave radiometers), but the backscattered SAR signal is in first order dependent on the geometric/structural properties of the target and in second order on its dielectric characteristics. Thus, effects resulting from vegetation cover (i.e., plant/leaf moisture) and surface roughness need to be considered for active soil moisture retrievals (Fluhrer et al., 2021; Hänsch et al., 2021; Kornelsen and Coulibaly, 2013). The simplified relation between soil moisture content and backscatter is positive, implying an increase in intensity with increasing moisture (Ulaby and Long, 2014).

In theory, the application of SAR data for the estimation of soil moisture is advantageous over sites with no or sparse vegetation coverage, e.g., in arid to hyper-arid environments, as this circumstance allows neglecting the influence of plant moisture and the scattering from vegetation on the SAR signal. This facilitates focusing the estimation of soil moisture (Bürgi and Lohman, 2021; Jordan et al., 2020; Yang et al., 2019), and/or surface roughness (Ezzahar et al., 2019; Sadeh et al., 2018; Sano et al., 1998; Ullmann and Stauch, 2020). However, large anomalies were observed for arid and hyper-arid environments across the globe from such active soil moisture retrievals (Dostálová et al., 2014; Morrison and Wagner, 2020; Wagner et al., 2022). Specifically, anticorrelations were observed over arid and hyper-arid sites characterized by a persistent or temporal increase in backscatter with decreasing moisture. These anomalies can reduce the value of global models on the soil moisture estimates and introduce errors and uncertainties in subsequent products (Morrison and Wagner, 2020; Wagner et al., 2022).

Recent research explains these anomalies in SAR data by subsurface reflections that can become the dominant return once the attenuation of a covering layer decreases. The occurrence of the effect is likely bounded to very dry soils and sedimentological settings allowing for a sufficient wavelength-dependent penetration of the SAR signal into/through the topsoil (Morrison, 2013; Morrison and Wagner, 2020; Wagner et al., 2022). Specifically, a buried consolidated layer, with significant roughness (e.g., bedrock, crusts), is overlaid by less or unconsolidated layer (e.g., sand or dust deposits). In dry state, microwaves can penetrate through the upper layer and scattering is dominantly caused at the buried layer. With increasing moisture, the attenuation of the upper surface layer increases and leads to a vanishing contribution of the backscatter from the buried layer. Ultimately, the signal is decreasing with increasing wetness of the top layer (Morrison, 2013; Morrison and Wagner, 2020).

Morrison and Wagner, 2020 have confirmed through laboratory experiments that such anomalies can arise from the presence of subsurface features. Importantly, their results indicated a dependency of subsurface scattering effects on soil moisture and soil structure, incidence angle, and polarization. The authors state that Sentinel-1C-Band data will have an increased sensitivity to these backscatter moisture anomalies (Morrison and Wagner (2020), p. 2197) and that above-mentioned dependency of polarization might provide diagnostics to identify locations prone to such anomalies. In fact, experiments of Morrison and Wagner (2020) indicate that cross-pol. returns were strongly associated with subsurface features, whereas co-pol. returns could be dominated by both surface and subsurface returns (Morrison and Wagner (2020), p. 2190). Recently Wagner et al. (2022) have presented global estimates on the occurrence of anomalous C-Band backscatter signals by investigating ASCAT soil moisture retrievals and modelled soil moisture data of ERA5-Land. They report negative relation between (modelled) soil moisture and C-Band backscatter over various arid regions across the globe (e.g., also northern Chile and the Atacama Desert, the Namib and Sahara Desert). Further, they note that subsurface scattering effects might also occur in more humid environments during dry spells. Wagner et al. (2022) conclude that this effect needs to be acknowledge in active soil moisture retrievals, and that further analysis of SAR time series on small-scale geomorphological patterns using field observations is required. While certainly limiting the value of active soil moisture retrievals, the identification of subsurface scattering from rather high resolution SAR imagery might support soil mapping efforts (Wagner et al., 2022).

In summary, the effect of subsurface scattering, its potential influence on active soil moisture retrievals and its occurrence in global ASCAT soil moisture retrievals were described in previous studies; however, its actual occurrence in recorded SAR data (e.g., Sentinel-1) is largely unknown. The objective of the study at hand is therefore to explore the sensitivity of C-Band backscatter time series of Sentinel-1 to near-surface soil moisture and its temporal dynamics within the hyper-arid environment of the Atacama Desert and to investigate the presence and occurrence of subsurface scattering effects leading to an anti-correlation with the soil moisture. For this purpose, time series from Sentinel-1 are compared with in situ soil moisture measurements available through a new network of meteorological stations and with in situ records of shallow sediment-profiles. The study investigates: (i) the direct relation between Sentinel-1 time series and near-surface soil moisture by comparing the backscatter values to in situ observations; (ii) the type of scattering and the potential occurrence of subsurface scattering effects; and (iii) the spatial patterns of seasonal varying Sentinel-1 intensities within the Atacama Desert.

2. Materials and methods

2.1. Study area - the Atacama Desert

The hyper-arid core of the Atacama Desert (Fig. 1) experiences <10 mm/year rainfall on average and thus is one of the driest places on Earth (Houston and Hartley, 2003). Factors leading to this pronounced hyperaridity are the coastal upwelling of the Peru-Chile Current (Rundel et al., 1991), the subtropical subsidence (Hartley et al., 2005), and the lee-effects of the Andes (Houston and Hartley, 2003). Consequently, the surface soils of the Atacama Desert are often dominated by gypsum and other salts (Arens et al., 2021; Voigt et al., 2020). Due to convective rainfall from tropical easterlies and the influence of southern westerlies (de Porras et al., 2017), the precipitation increases north-, east- and southwards of the hyper-arid core region. A main driver for increased humidity is the marine fog, which frequently occurs along the coastal margin and western slopes of the Coastal Cordillera below 1200 m above sea level (Cereceda et al., 2002; del Río et al., 2018). However, fog occurrence may extend inland depending on the local morphology (Cereceda et al., 2002). The annual water vapor variability reaches 30%

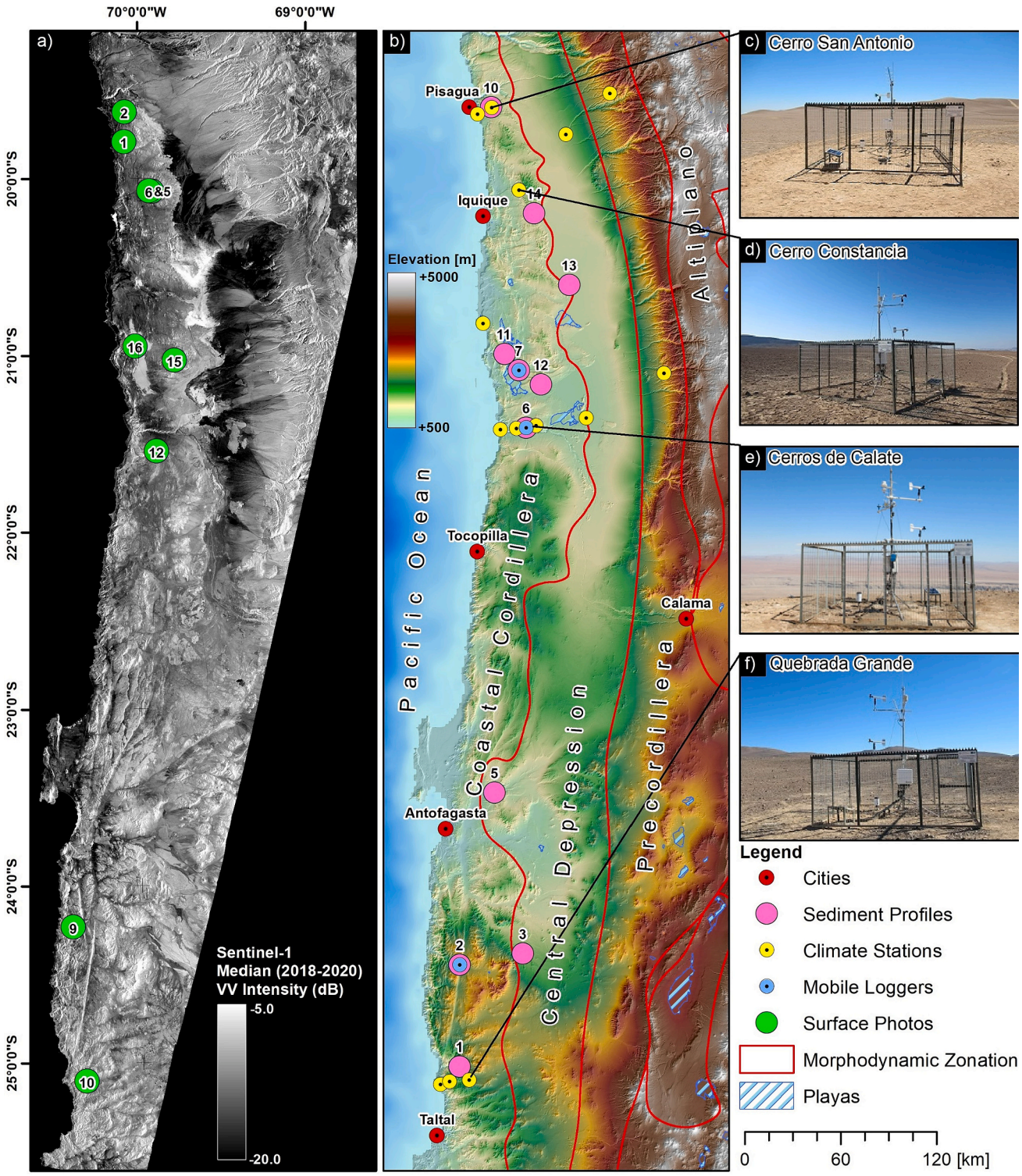

Fig. 1. Overview of the study area and available datasets: (a) median VV intensity (dB) calculated from Sentinel-1 time series acquired between January 2018 and December 2020. (b) Digital Elevation Model (GLO-90) of the study area and location of major cities, meteorological stations, surface photographs, sediment profiles, playas and general morphodynamic zones. (c-f) Photographs of meteorological stations (photos taken by D. H. & S. M. M.; accessible via *https://crc1211db.uni-koeln.de*).

and is correlated to ENSO (Böhm et al., 2020). Resulting from these processes, the driest parts of the Atacama are located between the coastal ranges and the pre-Andean cordilleras. Further, dryness expands to the Central Depression, which is confined in the east by the alluvial fan systems and in the west by the slopes of the Coastal Cordillera (Fig. 1).

Due to the hyperaridity, the geomorphic processes are taking place in remarkable slowness, which is evident by the age of surfaces and landforms (Clarke, 2006; Dunai et al., 2005; Matmon et al., 2015). Nevertheless, there are several records, especially from the last decade, that indicate that flash floods can even reach hyper-arid parts of the Atacama, e.g., events in 2015 (Jordan et al., 2018; Scott et al., 2017; Wilcox

et al., 2016), or 2017 (Lictevout and Gocht, 2018). Besides the fluvial morphodynamics, salt-driven shrink-swell, slumping, solifluction-type processes, or seismicity-driven processes, might be responsible for various landforms (Abele, 1990; Matmon et al., 2015; May et al., 2019; Quade et al., 2012). Smooth slope morphologies typically result from thick atmospherically derived salt and dust deposits, leading to soils containing large amounts of nitrate, iodate and sulphates gypsum and/or anhydrite (Ewing et al., 2006; Michalski et al., 2004; Rech et al., 2003; Voigt et al., 2020). Depending on its position, these soils show salt-cemented horizons (*costra*) frequently covered by a powdery layer of dust, with a typical thickness of 20–30 cm, and sulfate salts (*chuca*) (Ericksen, 1983; Latorre et al., 2013). The atmospheric deposition may lead to a remarkable volumetric expansion (up to 950% ±370% (Ewing et al., 2006)) under long-term hyperaridity and is thought to be supported by Biological Soil Crusts (Wang et al., 2017), while recent research indicates/speculates about the influence of soil moisture variations, as soil moisture in such soils varies due to evaporation and to vapor fluxes at the air–soil interface (Böhm et al., 2020; Shao et al., 2021).

2.2. Data

2.2.1. Sentinel-1 time series (2018–2020)

Sentinel-1 GRD imagery was processed using the Google Earth Engine (Gorelick et al., 2017) for the period from 01 January 2018 to 31 December 2020. All Sentinel-1 datasets were acquired in descending orbit (orbit 54) and at 10:08 UTC. In total 176 GRD mosaics were obtained. These mosaics had a native pixel size of 10 m by 10 m, were converted to linear scale, and then filtered using a boxcar filter with a size of 3 by 3 pixels. Afterwards, data was resampled to a pixel size of 80 m by 80 m using bilinear interpolation and was then transformed to decibel (dB) units. The resampling to 80 m was done to (i) reduce the data-load, considering the large study area, and (ii) to increase the radiometry of the signal. For all acquisitions, both polarization channels (VV & VH) were available. Prior to the analyses, the mosaics of VV and VH were cropped and resampled to a common grid using UTM projection Zone 19 South and the WGS 1984 ellipsoid (EPSG:32719). VV and VH intensities were finally extracted for all stations (see below).

2.2.2. Meteorological stations and in situ soil moisture measurements

In situ measurements of soil moisture were conducted by a network of 14 permanently recording meteorological stations and measurements of soil moisture by three temporary stations on selected locations (see Fig. 1). The meteorological station network (type: Campbell Scientific Inc.) was established between 2017 and 2018 to fill the observational gap in the Atacama Desert (details provided in Schween et al. (2020)). The raw data is freely available (*https://crc1211db.uni-koeln.de*) (Hoffmeister, 2018). The network currently consists of three transects in the north (~19.7°S), center (~21.5°S) and south (~25°S) of the Atacama, each ranging from the coast to the slope of the Andes (see Fig. 1). Besides measurements of standard meteorological parameters (e.g., temperature, humidity), each station is additionally equipped with further sensors (e.g., soil surface temperature). Particularly, each station also records soil moisture by at least one CS616 sensor of Campbell Scientific Inc. in 10 cm depth (*https://www.campbellsci.com/cs616-reflectometer*), specifically designed for measurements of the volumetric water content from 0% to saturation in soft soil. In addition, temporary stations (type: Ecotech GmbH) were used to monitor soil moisture by TRD-type SMT-100 sensors (UGT/ Ecotech) in 10 cm depth at three locations (Paposo Fault (Zebra Stripes), Salar Grande (Sediment Lobes) and Rio Loa (Patterned Ground)). All meteorological stations provided hourly temperature-corrected measurements of the near surface soil moisture (in %; volumetric water content). The measurements closest to the acquisitions of the Sentinel-1 data (see section 2.1) were extracted and further analyzed.

2.2.3. Auxiliary data

A collection of 19 georeferenced field photographs, collected during fieldwork in 2017, 2018 and 2021, was available, along with information from 13 shallow sediment profiles (see Fig. 1), also collected in 2017, 2018 and 2021. The sediment profiles provided descriptive information on the structure and grain size composition down to a minimum depth of approx. 30 cm. In addition, the GLO-90 digital elevation model (Copernicus Global Digital Elevation Model) was available for the entire study area (see Fig. 1 and "Data Availability Statement"). It was resampled to UTM projection Zone 19 South and the WGS 1984 ellipsoid (EPSG:32719) with a spatial resolution of 80 m, matching the resolution of the Sentinel-1 data.

2.3. Methods

Recent research (Böhm et al., 2020; Shao et al., 2021) suggests seasonal variations in near-surface soil moisture in the Atacama Desert due to seasonal varying humidity (i.e., without the occurrence of precipitation). Such variations are, on the long-run, potential drives for land surface dynamics. The initial analyses of the Sentinel-1 time series and of the soil moisture measurements, confirmed the presence of seasonal variations over selected locations in the hyper-arid core of the Atacama Desert (Fig. 2). Identifying a significant correlation between the SAR time series of Sentinel-1 and the near-surface soil moisture would, therefore, allow to map and identify locations showing seasonal variations of humidity. It would also enable to extrapolate the presence of seasonal changing near-surface soil moisture conditions for the entire study area at comparable high spatial resolution. Consequently, two assessments were applied in this study; (i) the relationship between Sentinel-1 VV/VH intensities and the volumetric soil moisture measured in situ at the stations was investigated; (ii) the Sentinel-1 time series was analyzed, and seasonal variations of intensities were identified using a simple but efficient non-linear least squares fit to a pre-defined sine function.

2.3.1. Correlation and regression of Sentinel-1 to in situ soil moisture measurements

The Sentinel-1 time series was compared to the near-surface soil moisture values (%) measured at the stations. For this task, the temporally corresponding soil moisture measurements were extracted at the overflight time of Sentinel-1 (the number of samples per station is provided in Table 1). For each location, four values were extracted: VV (dB), VH (dB), VH-VV (dB), and the near surface soil moisture (%). Subsequently, the intensities were plotted versus the soil moisture measurements and strength and goodness/quality of the linear fit was estimated using the Pearson Correlation Coefficient (R), the Coefficient of Determination (R^2) and the Mean Absolute Error (MAE). The significance of the correlation was assessed using the *p*-value and correlations were assigned signification if p-value was lower 0.05.

2.3.2. Characterization of seasonal variations in Sentinle-1 time series

The second analyses aimed to identify locations in the Sentinel-1 time series that exhibit a seasonal characteristic, as SAR intensity is potentially related to the above-mentioned seasonal variations in near-surface soil moisture. To facilitate comparison between stations, the extracted Sentinel-1 time series of each locality/pixel were normalized (i.e., the arithmetic mean was calculated and subtracted from all measurements). As exemplified in Fig. 2 a, the initially found (normalized) signal variations follow a seasonal fluctuation, which can be described approximatively with a simple sine function with a wavelength of one year (Eq. 1). This function was fitted to the normalized Sentinel-1 time series of each pixel, using the MPFIT function (Markwardt, 2009) in the software IDL (*https://www.l3harrisgeospatial.com*) and the constraint that amplitude A is greater zero.

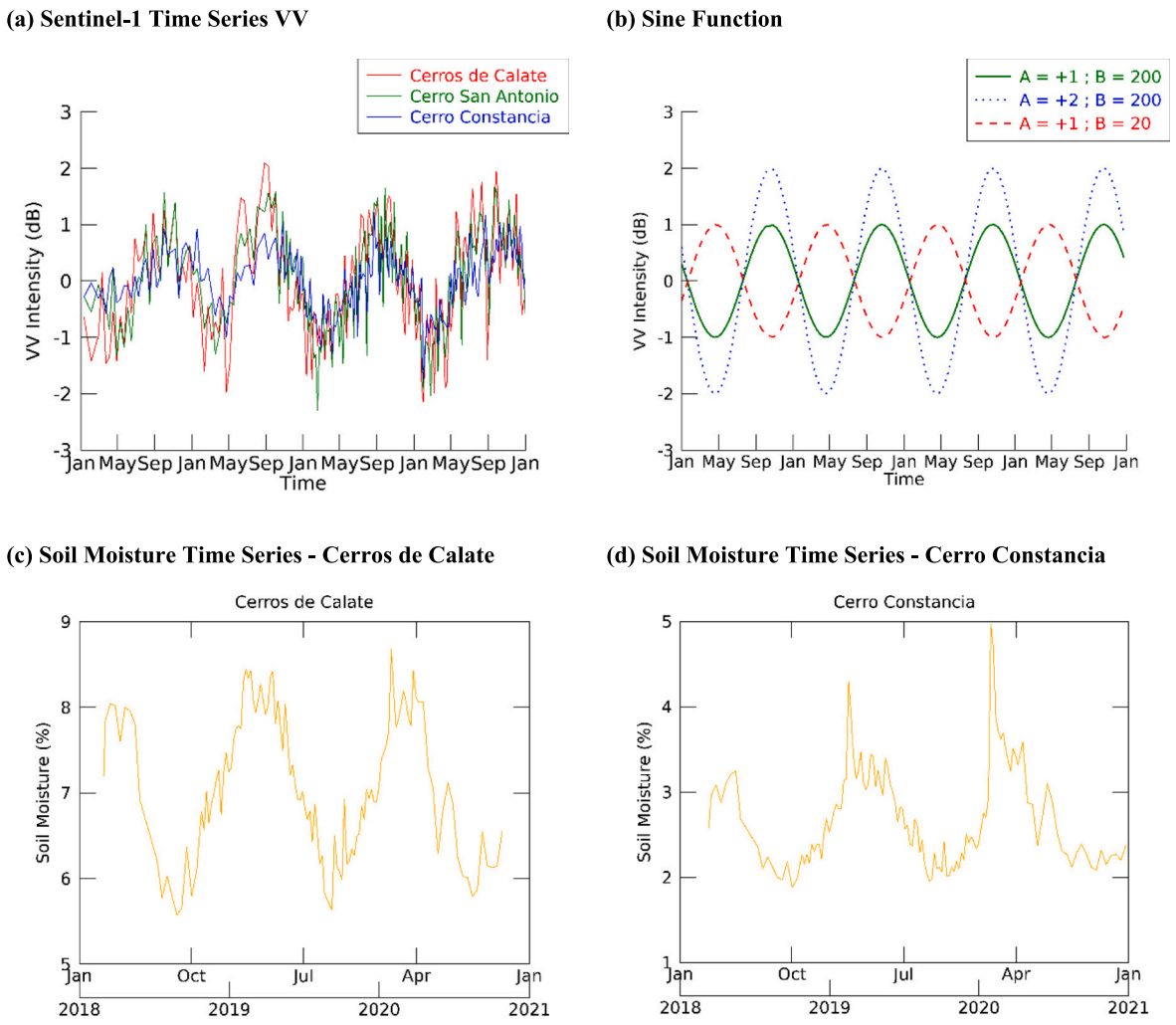

Fig. 2. Examples on seasonal variations of remote sensing as well as in situ signals and their modelling: (a) seasonal variations in Sentinel-1 VV intensity at selected locations with meteorological stations that were observed during the initial analysis, (b) examples on a generic sine function defined by parameters A (Amplitude) and B (Phase) (see Eq. 1), and (c-d) examples on seasonal soil moisture variations measured in situ at the meteorological stations Cerros de Calate and Cerro Constancia.

Table 1
Relation/correlation between Sentinel-1 features (VV (dB), VH (dB) and difference between VH and VV (VH-VV)) and Soil Moisture (SM) (%) (see Fig. 1). R refers to the Linear Pearson Correlation Coefficient and MAE denotes the Mean Absolute Error (in dB), n denotes the number of samples, and β denotes the slope of the linear model. Entries with $R^2 > 0.5$ are significant (p-values <0.05). Stronger correlations indicate a better linear relation between SM and the Sentinel-1 feature. Entries with $R^2 > 0.5$ are marked in bold. Asterisk (*) denotes in situ data from mobile loggers, while all other SM in situ data were collected at meteorological stations (see Section 2.2.2.). "Caleta S.d.P. Grande" denotes the station "Caleta Sur de Punta Grande".

Station	n	SM (%) vs. VV (dB)				SM (%) vs. VH (dB)				SM (%) vs. VH-VV (dB)			
		R	R^2	MAE	β	R	R^2	MAE	β	R	R^2	MAE	β
Caleta Loa	80	0.53	0.28	0.32	1.64	0.00	0.00	0.36	0.01	−0.47	0.23	0.36	−1.63
Rio Loa	132	0.04	0.00	0.19	0.15	0.27	0.07	0.57	3.03	0.27	0.07	0.52	2.88
Cerros de Calate	127	−0.87	**0.76**	0.33	−0.95	−0.92	**0.84**	0.40	−1.44	−0.83	**0.70**	0.20	−0.50
Salar de Llamara	132	−0.19	0.03	0.21	−0.25	0.20	0.04	0.72	0.89	0.26	0.07	0.74	1.14
Quebrada de Mani	132	0.08	0.01	0.31	0.00	−0.52	0.27	0.28	−0.02	−0.43	0.19	0.40	−0.02
Alto Patache	125	−0.01	0.00	0.25	0.00	−0.15	0.02	0.36	−0.06	−0.20	0.04	0.24	−0.06
Caleta Junin	132	−0.01	0.00	0.17	0.00	−0.36	0.13	0.44	−0.01	−0.43	0.18	0.37	−0.01
Cerro San Antonio	132	−0.72	**0.52**	0.42	−4.29	−0.69	0.47	0.70	−6.30	−0.57	0.33	0.30	−2.00
Cerro Constancia	132	−0.89	**0.79**	0.18	−0.80	−0.88	**0.77**	0.35	−1.43	−0.79	**0.63**	0.22	−0.63
Quebrada de Aroma	100	−0.75	**0.56**	0.20	−0.98	−0.87	**0.75**	0.28	−2.32	−0.81	**0.66**	0.21	−1.34
Quebrada de Soga	132	−0.26	0.07	0.15	−0.01	−0.67	0.45	0.27	−0.03	−0.71	0.49	0.20	−0.03
Rio Loa *	44	0.03	0.00	0.19	0.03	0.25	0.06	0.33	0.56	0.26	0.07	0.30	0.53
Salar Grande *	44	0.23	0.05	0.17	0.55	0.38	0.14	0.35	1.92	0.38	0.15	0.24	1.37
Caleta S.d.*P. Grande*	67	0.55	0.31	0.18	0.12	0.11	0.01	0.19	0.02	−0.55	0.30	0.15	−0.10
Quebrada Matancilla	132	−0.61	0.37	0.12	−0.46	−0.47	0.22	0.23	−0.57	−0.12	0.01	0.21	−0.11
Quebrada Grande	132	−0.23	0.05	0.12	−0.26	−0.43	0.18	0.24	−0.97	−0.38	0.14	0.20	−0.71
Paposo Fault *	105	0.04	0.00	0.20	0.01	−0.06	0.00	0.39	−0.03	−0.11	0.01	0.27	−0.04

$$f(X) = A^{*}sin(\omega t + \varphi) = sin\left(\frac{X - B}{365.25}{*}2\pi\right){*}A \quad (1)$$

In Eq. (1), X is the variable for the scenes in the time series, while parameters A and B describe the shape of the sine function (Fig. 2b). Thereby, A is the amplitude of the function (in dB), while parameter B defines the phase shift of the function (in days). In the subsequent analyses, parameter B was further adapted to indicate the day of year (DOY) at which the maximum amplitude of the function is reached. To avoid confusion, this parameter is referred to as B_{MAXDOY} in the following (i.e., B_{MAXDOY} indicates the annual phase lag of the phenomenon). The goodness of fit between the modelled sine function and the time series under investigation (i.e., either VV (dB), VH (dB), or VH-VV (dB)) was estimated using R, R^2 and MAE. As result of this modelling, four layers (same extent as in Fig. 1 a) indicating R^2, MAE, parameter A, and parameter B_{MAXDOY} were determined per pixel for VV (dB) and VH (dB) (see Section 3.2). These parameters describe the best fitting sine function. Finally, the same fitting was applied to the point-wise time series of the soil moisture (i.e., for all stations/loggers) to indicate whether a seasonal sine function applies to the in situ record or not.

3. Results

3.1. Relation/correlation of Sentinel-1 and near-surface volumetric soil moisture

The comparison of the Sentinel-1 VV, VH and VH-VV intensities revealed for most stations no significant linear relation ($R^2 < 0.5$) to the soil moisture (Table 1, Figs. 3 & 4). However, exceptions were found for the stations Cerros de Calate, Cerro San Antonio, Cerro Constancia (located in the uplands of the Costal Cordillera and within the core of the desert) and Quebrada de Aroma (located at transition between the Central Depression and the Precordillera). These showed R^2 values greater 0.5 up to a maximum of around 0.84 (exemplarily illustrated in Fig. 3 a-d for the station Cerros de Calate; other scatterplots provided in Fig. A1 & A2). Notably, (i) all significant relations ($R^2 > 0.5$ and $p < 0.05$) between SAR intensities and soil moisture measurements were negative; (ii) correlations were in most cases slightly higher in VH than in VV (Fig. 3 and Table 1); (iii) the difference between VH and VV correlated with the volumetric soil moisture, but at a lower level as the intensities; (iv) small changes in near-surface soil moisture (e.g. differences of around 3.2% for Cerros de Calate) led to high changes in backscatter (e.g. up 3.5 dB in VV, up to 5 dB in VH for Cerros de Calate, see Fig. 3 and Table 2).

For some stations, partially positive and negative relations were found, indicating a non-linear and complex relationship when looking at the entire series. This is exemplarily illustrated in Fig. 3 e-h for the station Quebrada de Soga, which experienced two rainfall events in 2019 and 2020 causing strong changes in soil moisture. Here, the scatterplots of VV, VH and VH-VV reveal a complex response of the Sentinel-1 intensities to the increase or decrease in near-surface soil moisture. While the relation between moisture and intensity is negative for soil moisture values between 10% and 25%, a positive relation in VV (and less strong in VH) is visible for soil moisture values above ca. 25%. Noticeably, VH-VV reveals a complex relation, as such as there seemed to be at least two different modes, best visible for soil moisture values between approx. 15% and 30%.

3.2. Mapping of seasonal variations of Sentinel-1 backscatter and in situ soil moisture

The sine function fitting outlined in section 2.3.2. was conducted for the Sentinel-1 time series (VV, VH, VH-VV) and for the soil moisture measurements collected at the meteorological stations and soil moisture loggers. For each fitting, the parameters R^2, MAE, parameter A, and B_{MAXDOY} were noted and analyzed. Fig. 4 provides a graphical summary of the main findings, which are as follows: (i) highest agreement in seasonal cycling between SAR features and soil moisture was found for stations having a high relation between SAR intensities and soil moisture ($R^2 > 0.6$); (ii) the agreement was strongest for sine functions with an amplitude (A) >0.6 dB (i.e., the range of the full cycle is twice that value and therefore exceeding a seasonal variation of 1.2 dB) (see Fig. 4 a&c); (iii) the agreement was more pronounced in VH and VV, but less strong in VH-VV (see Fig. 4 e); (iv) a shift of around 180 days was found between B_{MAXDOY} values of VV, VH and VH-VV and B_{MAXDOY} values of the soil moisture measurements, indicating that the maximums of the respective time series are roughly shifted by half a year (see Fig. 4 b, d & e), this was best pronounced for sine functions showing parameter A >0.6 dB. Based on these findings the results of the sine fitting were mapped for the entire study area and for the sine fitting parameters of the VV and VH time series (shown in Fig. 5). Results indicated a spatially variable R^2 value in both polarizations. R^2 was generally lower in closer proximity to the coast and for most regions within the Central Depression. Further, there were higher R^2 values in the north of the study area, whereas regions further south tend to have lower R^2 values (Fig. 5 a&b).

Parameter B_{MAXDOY} was for most parts of the region rather homogenous and around 200–260. This observation compares well with the Sentinel-1 B_{MAXDOY} values of the meteorological stations (see Fig. 4 d&e). Noticeable exceptions were found over the alluvial plains and fans of the Central Depression (B_{MAXDOY} around 50 to 80), the Salar Grande (B_{MAXDOY} around 360 to 40), and along the coast (best resolved in VV with B_{MAXDOY} around 120 to 180). Notably, the amplitude (A) (Fig. 5 g&h) of the sine fitting clearly indicated stronger seasonal variations in the north of the study area, especially over the northern Coastal Cordillera and some alluvial fan surfaces situated at the transition between the Central Depression and the Precordillera. The amplitude (A) of the sine fitting was generally higher in VH compared to VV, potentially as it has a higher dynamic range for subsurface scattering effects (see *4. Discussion*).

Taking these observations and the findings of the initial assessment on the sine function fitting further (see Fig. 4 and its description), parameters B_{MAXDOY}, R^2 and A were compiled in a single map. Doing so, pixels showing $R^2 < 0.6$ and A< 0.5 dB were masked out. This was done to focus on sites that show (i) at least a medium strong correlation ($R^2 > 0.6$) (Fig. 4) and (ii) a seasonal signal variation exceeding the suspected minimum variation induced by speckle and noise (El Hajj et al., 2016; Schmidt et al., 2020; Ullmann et al., 2019). This mask was superimposed to B_{MAXDOY} (Fig. 6 a&b). The generated maps show a distinct anomaly in VV and VH that stretches north to south and is located in the central uplands of the Coastal Cordillera. It is roughly limited in the north by the meteorological station Cerro San Antonio and in the south by the station Cerros de Calate This anomaly is also evident when just focusing on the R^2 values of the sine fitting (Fig. 6 c&d).

Sediments within this region (Figs. 7 & 4. *Discussion*) are characterized by thick atmospherically derived dust deposits and cemented crusts underneath the dust deposits. The western border of the anomaly corresponds well with the 1000 m a.s.l contour line, which is close to the upper limit of the maritime fog. Among the processed contour lines (100 m equidistant), the 1000 m a.s.l contour was corresponding best with the western border of the anomaly. To the east the anomaly is bounded by the transition from the Coastal Cordillera to the Central Depression. Both polarizations indicate rather homogeneous B_{MAXDOY} values of around 240, except for the Salar Grande (B_{MAXDOY} around 360 to 40). Notably, in VH also several alluvial fans at the border between the Central Depression and the Precordillera are indicated to have a strong seasonality ($R^2 > 0.6$ and A> 0.5 dB) with B_{MAXDOY} values of around 240, e.g., the fan system located between Cerro San Antonio and Quebrada de Soga (Fig. 6). These are not, or to a lesser extent, found in the VV anomaly map.

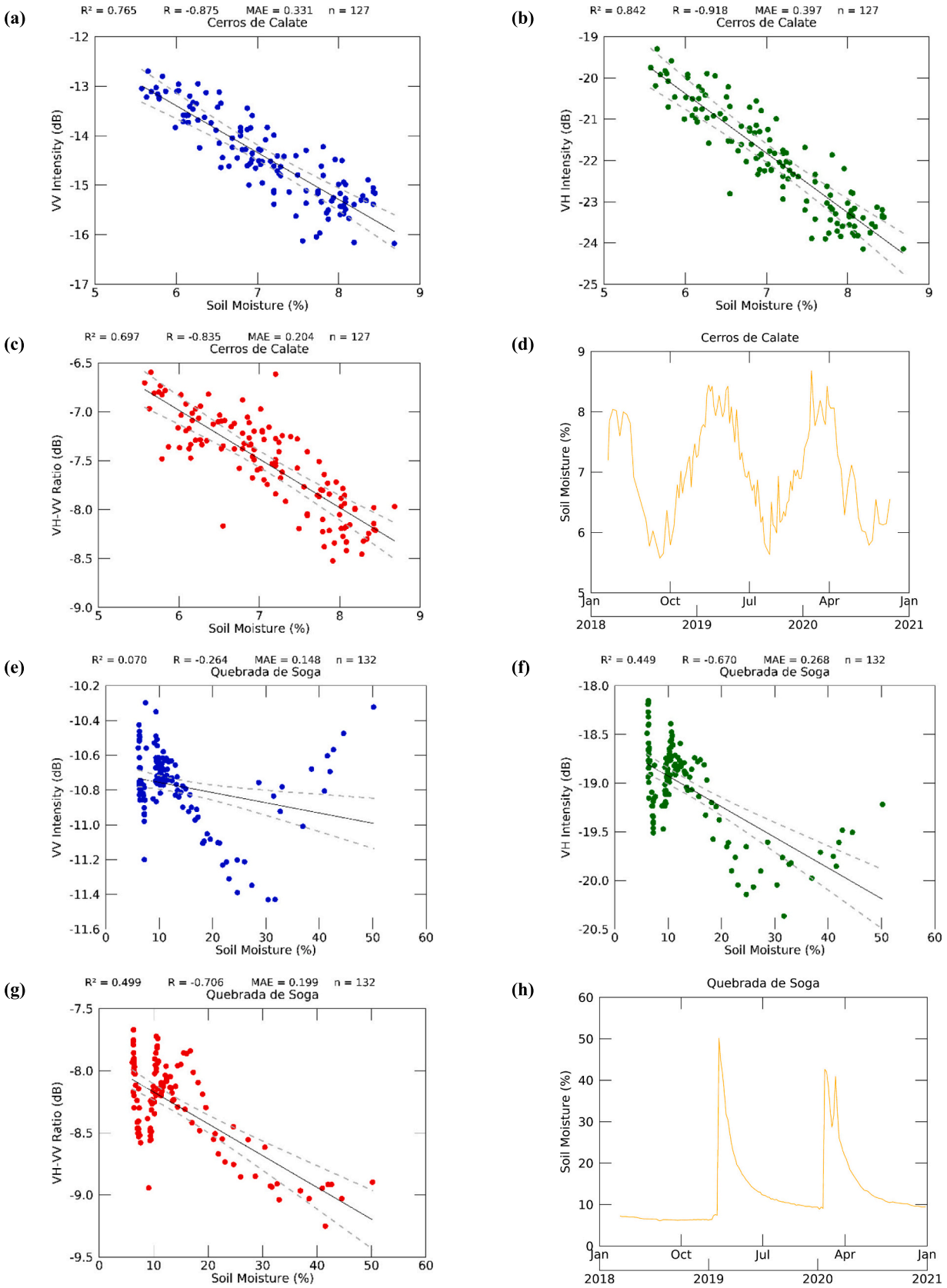

Fig. 3. Correlation between Sentine-1 time series and near-surface (in situ) soil moisture for the meteorological stations Cerros de Calate (a-d) and Quebrada de Soga (e-h): (a&e) soil moisture (%) vs. VV intensity (dB), (b&f) soil moisture (%) vs. VH intensity (dB), (c&g) soil moisture (%) vs. VV-VH intensity (dB), and (d&h) time series of the soil moisture (%). R indicates the Pearson Correlation Coefficient, R^2 the Coefficient of Determination, MAE the Mean Absolute Error and n provides the number of valid samples. Grey dashed lines draw the lower and upper limit of the 95% confidence interval of linear regression. Scatterplots of Cerro Constancia, Cerro San Antonio and Quebrada de Aroma are provided in Fig. A1 and Fig. A2 (Appendix).

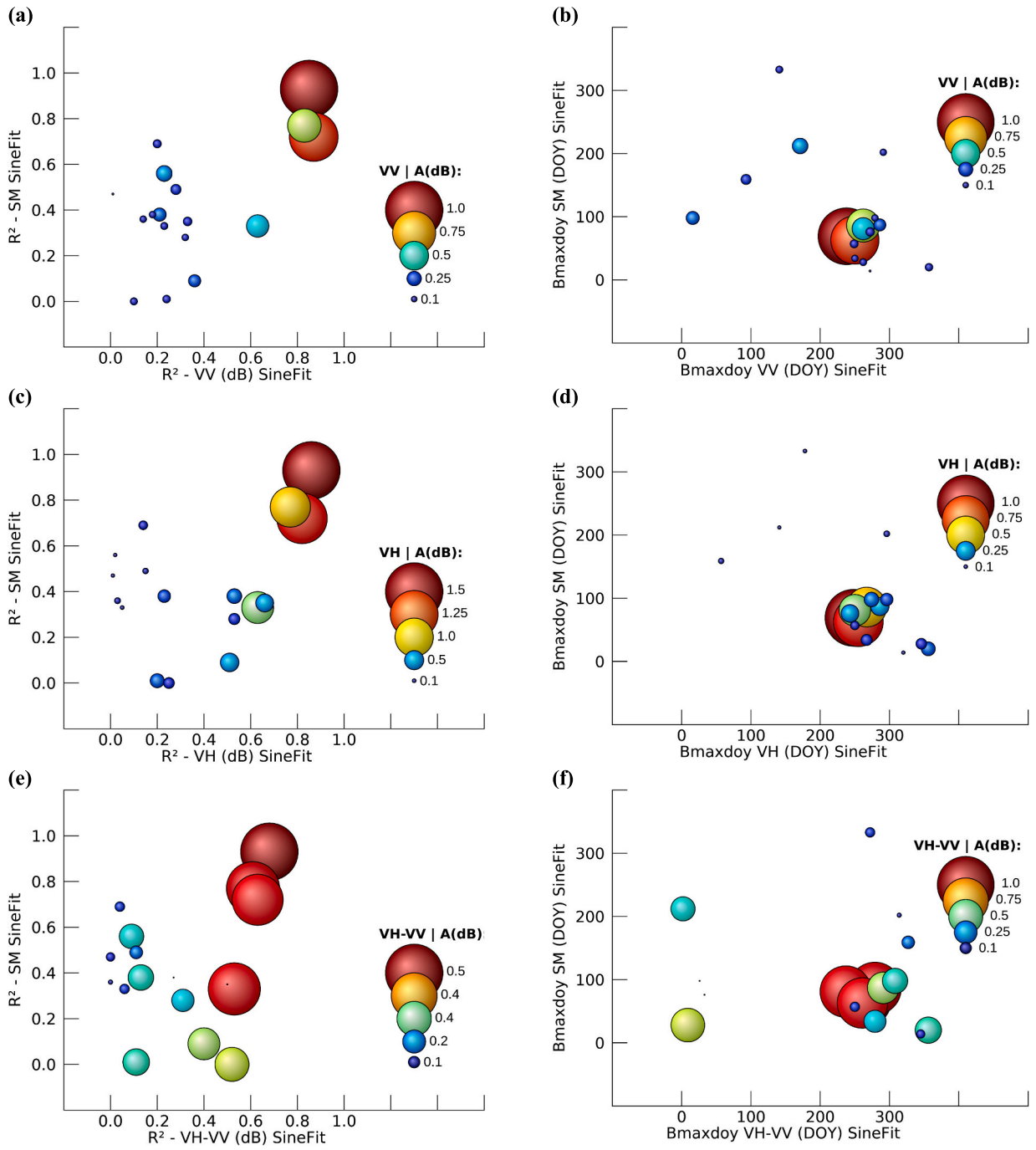

Fig. 4. Comparison of parameters deduced from the sine function fitting (see Section 2.3.2.). (a,c,e) Plots relate the Coefficient of Determination (R^2) (i.e., how well the function fitted the observation) of the time series (2018–2020) of VV, VH, VH-VV and of the soil moisture (SM) records. (b,d,e) Comparison of parameters B_{MAXDOY}, indicating the day of year (DOY) at which the maximum of the function (A; amplitude) is reached for VV, VH, VH-VV and of the soil moisture (SM) records. The diameters of the bubbles correspond to parameter A (dB).

Table 2
Range of Soil Moisture (SM) (%) and Sentinel-1 features (VV & VH (dB) and difference between VH and VV (VH-VV)) for selected meteorological stations (see Fig. 1, Fig. 3, Fig. A1 & A2) showing a linear relation with a Coefficient of Determination (R^2) above 0.5 (see Table 1) between January 2018 and 2020. The table denotes the observed minimum (min), maximum (max), standard deviation (sd), and the resulting range (span) for SM, VV, VH and VH-VV.

	SM (%)			VV (dB)				VH (dB)				VH-VV (dB)		
Station	min	max	span	min	max	span	sd	min	max	span	sd	min	max	span
Cerros de Calate	5.5	8.7	3.2	−16.5	−12.5	4.0	0.86	−24.5	−19.0	5.5	1.26	−8.0	−6.5	1.5
Cerro San Antonio	0.82	1.65	0.83	−14.7	−11.7	3.0	0.74	−23.0	−18.0	5.0	1.13	−8.3	−6.3	2.0
Cerro Constancia	1.9	5.0	3.1	−15.0	−12.7	2.3	0.51	−24.5	−20.5	4.0	0.93	−9.5	−7.8	1.7
Quebrada de Aroma	2.1	3.9	1.8	−14.5	−12.5	2.0	0.39	−24.0	−20.0	4.0	0.80	−9.5	−7.5	2.0

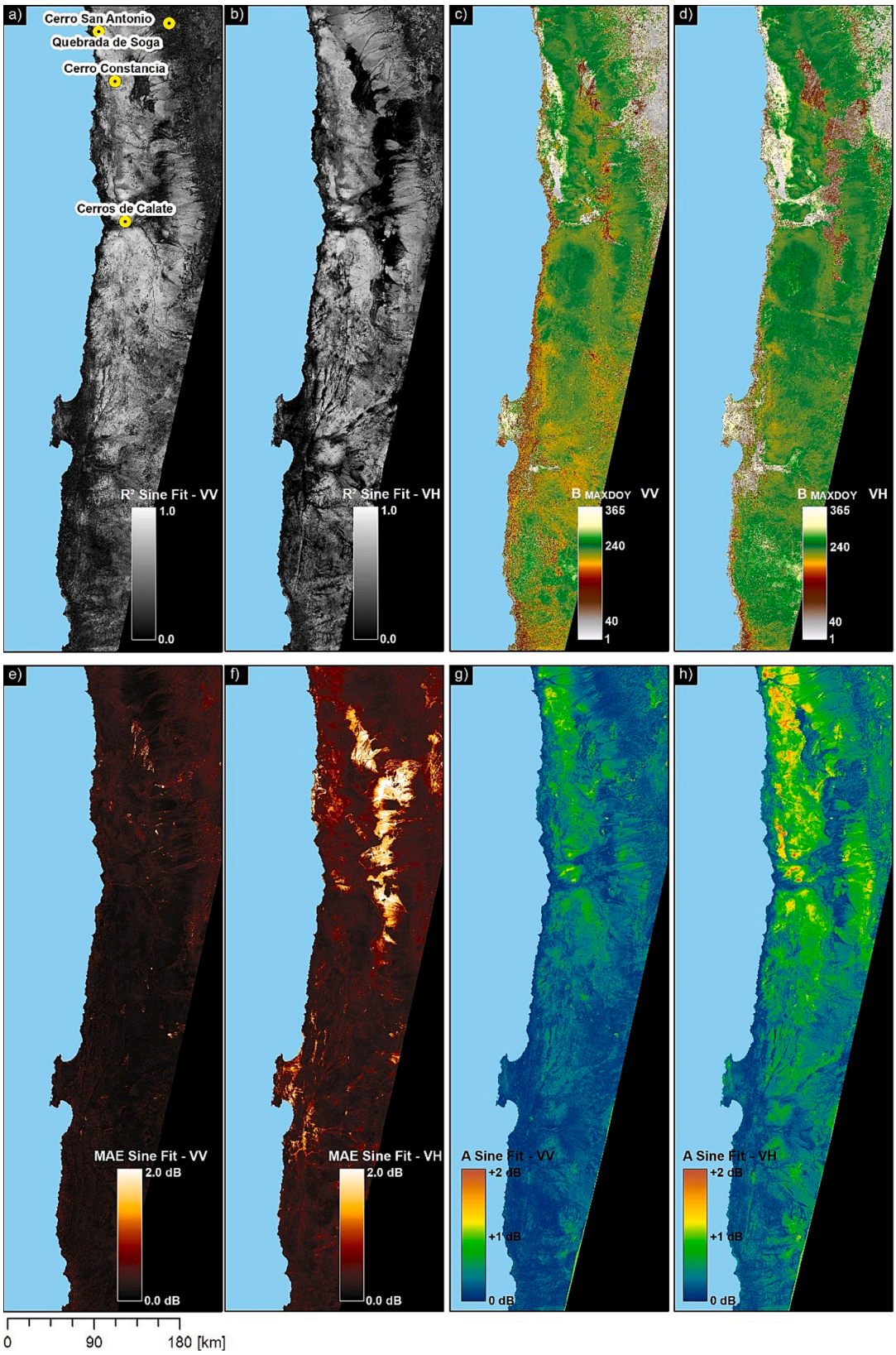

Fig. 5. Results of the sine fitting: (a-b) Pixel-wise Coefficient of Determination (R^2), (c-d) pixel-wise day of the year (DOY) at which the maximum amplitude (A) of the sine fit is reached (B_{MAXDOY}), (e-f) pixel-wise Mean Absolute Error (MAE) of the sine fit, and (g-h) pixel-wise amplitude (A) of the sine fit. Sine fitting was processed for VV and VH and for the entire time series (2018–2020).

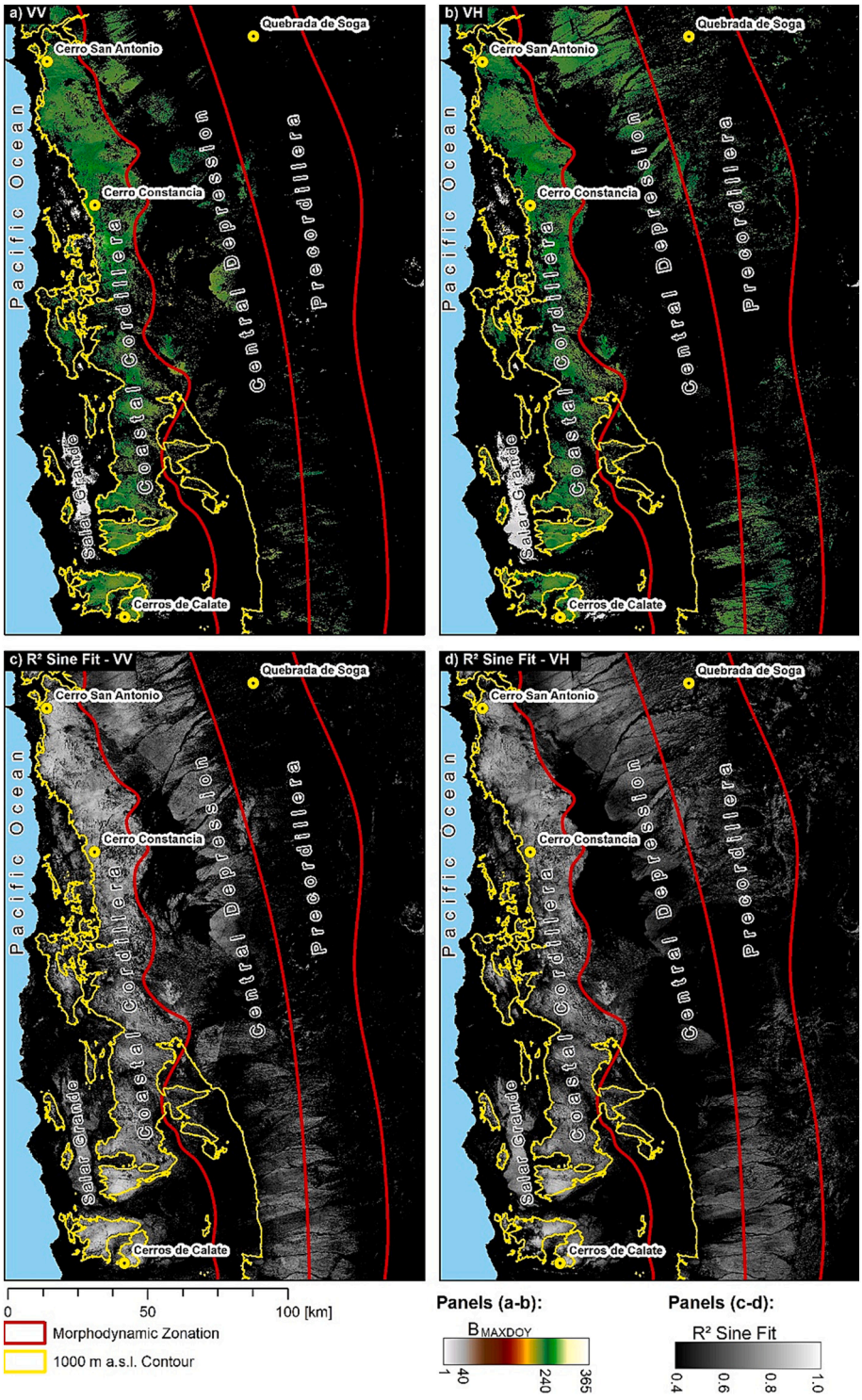

Fig. 6. Characterization of seasonal signal variations in the Sentinel-1 over the entire time series (2018–2020) for the northern part of the study area, the 1000 m above sea level (a.s.l) contour and the morphodynamic zonation. Figures (a) and (b) show the day of the year (DOY) at which the maximum amplitude (A) of the sine fit is reached (BMAXDOY) for VV and) VH. Areas with a Coefficient of Determination (R^2) lower 0.6 and with A< 0.5 dB (i.e., range of the sine function lower than 1 dB within one year) are masked out (black color). Figure (c) and (d) show the R^2 Sine Fit images of VV and VH.

4. Discussion

4.1. Relation of Sentinel-1 and near-surface volumetric soil moisture

Comparison of Sentinel-1 intensities and near-surface soil moisture revealed strong negative linear correlations over the driest parts of the Atacama Desert, as indicated by the comparison of the SAR time series with in situ soil moisture data (measured at 10 cm depth) of stations Cerros de Calate, Cerro San Antonio, and Cerro Constancia. The reason for this inverse relationship is interpreted to be caused by subsurface scattering effects, as over these sites a simplified two-layer scheme can be assumed; an upper layer consisting of the rather smooth fine-grained unconsolidated dust deposits and a lower layer characterized by the more rugged cemented crust (Ericksen, 1983; Latorre et al., 2013; May et al., 2020) (Fig. 7; upper left panels). In dry state, microwaves can penetrate through the first layer and scattering is dominantly caused at the (rougher) cemented crust. With increasing moisture (due to seasonal vapor fluxes from the atmosphere to the soil) the first layer causes an increasing attenuation, leading to a lower influence of reflections at the dust/crust-boundary on the SAR signal and, therefore, to a decreasing

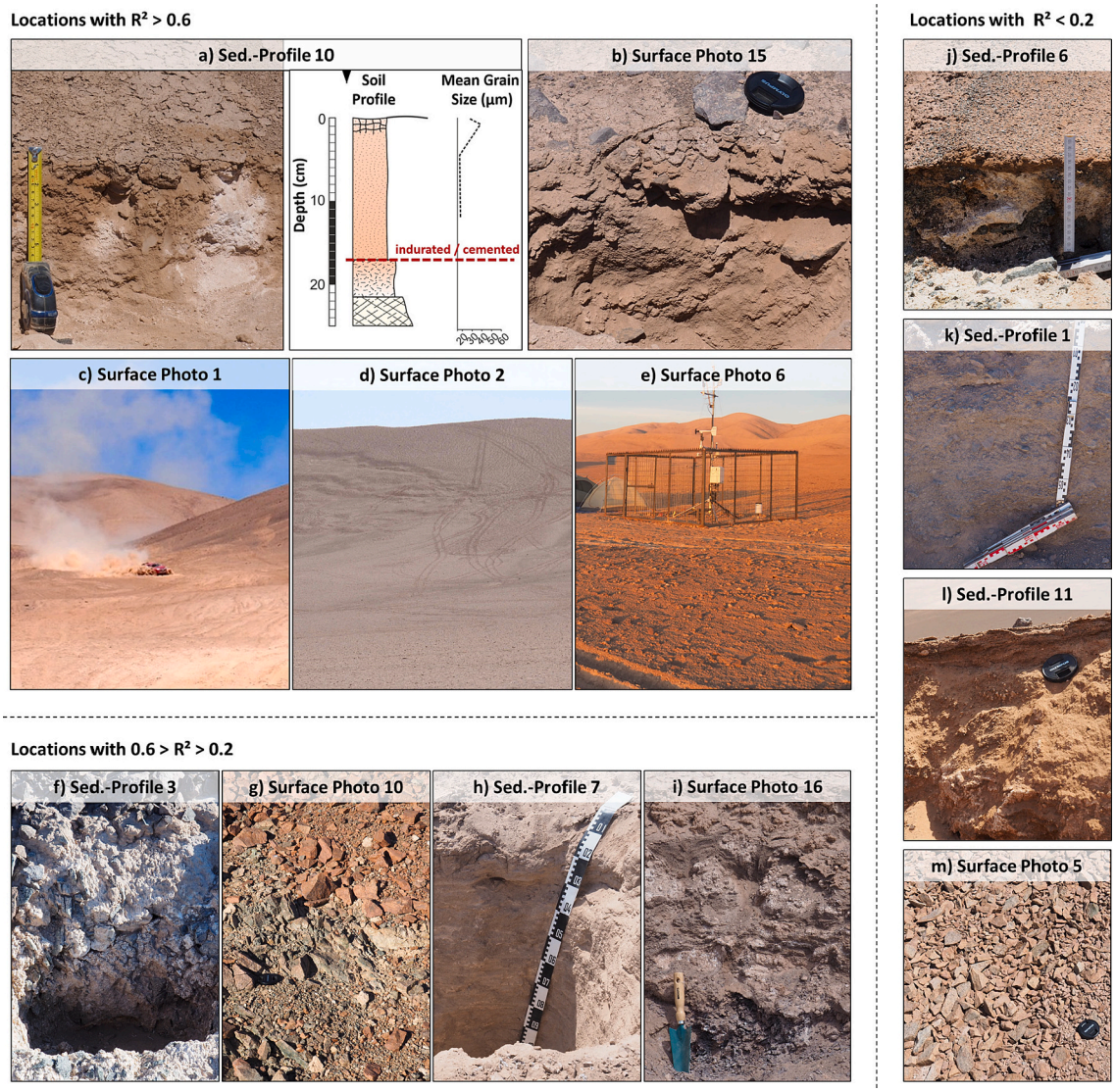

Fig. 7. Surface photos and sediments profiles (cf Fig. 1) in relation to the found seasonality (ref. Table 3) in the VV and VH time series of Sentinel-1. (a) Photo and schematic drawing of sediment profile 10 with results of mean grain size measurements. Below 15–18 cm b.s., a salt-indurated crust hinders further digging. Note large gypsum nodules surrounded by loose silt-dominated sediment (atmospheric dust) in the upper 15 cm. (b) Uppermost 15 cm of an old alluvial fan surface with few angular clasts at the surface; the subsurface sediment is dominated by loose homogenous silt with few clasts; note lens cap as scale. (c) Car tracks (and car struggling) in dusty sediment cover (*chuca*), which is typically ~20 cm thick in this central part of the northern Coastal Cordillera (between Iquique and Pisagua). (d) Car tracks in the 15–20 cm-thick *chuca* layer, central Coastal Cordillera, Pisagua area. (e) Car tracks in the 15–20 cm-thick *chuca* layer around meteorological station Cerro Constancia, central Coastal Cordillera, Iquique area. (f) Photo of sediment profile 3, which has originally been described by Owen et al. (2013). Indurated salt and gypsum layers directly underlie a clast-dominated (zebra-striped) surface. Clasts at surface are ~3–5 cm large. (g) Angular clasts overlying fragmented bedrock in the Coastal Cordillera, Paposo area; note lens cap as scale. (h) Sediment profile 7, which has originally been described by May et al. (2020) (May et al., 2020, 2019). The 140-cm thick sediment profile is well stratified, sand-rich and has no indurated salt or gypsum crust-type layer. (i) Small outcrop west of Salar Grande showing fragmented bedrock at the base covered by partly indurated salt and gypsum layers/nodules; the uppermost ~10 cm consist of fine-grained and slightly indurated atmospheric dust deposits, covered by a thin surface crust. (j) Shallow sediment profile just north of Rio Loa canyon with <5 cm fine-sediment cover (red) and a thick gypsum and salt crust overlying shattered bedrock. (k) Sediment profile in an inactive section of an alluvial fan in the Coastal Cordillera close to Paposo; the profile entirely consists of poorly stratified sediment dominated by gravel in a sandy matrix. (l)) Upper section of a sediment outcrop west of the Salar Grande, at the foot slope of the western part of the Coastal Cordillera (Medialdea et al., 2020). The uppermost part of the 6-m high outcrop consists of non-indurated heterogeneous colluvial material (i.e., a mixture of sand, silt and fine angular gravel). (m) Clast-covered surface in the central Coastal Cordillera, Paposo area. All photos taken by S. M.M., D.H., and O.B. (For interpretation of the references to color in this figure legend, the reader is referred to the web version of this article.)

backscatter with increasing soil moisture. This interpretation is supported by the field photographs and the soil profiles (Fig. 7 and Table 3) and generally in line with the experiments by Morrison and Wagner (2020). Sites with strong linear correlation ($R^2 > 0.6$) (Fig. 6 c&d) are characterized by loose atmospheric dust deposits in the top soils and the presence of buried cemented crusts. Sites where clast-rich layers occur at the surface, and where *chuca* layer is absent, (Fig. 7; e.g., Sed.-Profile 3 & 6, Surface Photo 5 & 10) or with missing sub-surface cemented crusts (Fig. 7; Sed.-Profile 7) show weaker linear correlations ($R^2 < 0.6$) and no clear relation between the SAR signal and the near-surface moisture content. It needs to be considered that above mentioned sites exhibiting strong negative correlations are situated in geomorphological domains where active morphodynamics are taking place with remarkable slowness (see 2.1 Study Area). Therefore, constant roughness conditions over time can be assumed over these sites. Considering the seasonal nature of the observed variations, we interpret changes in dielectric properties to

Table 3
Assessment of the sine fits for Sentinel-1 time series of VV and VH for selected locations with ground reference (surface photos or soil profiles, see Fig. 7). R^2 refers to the Coefficient of Determination. B_{MAXDOY} denotes the day of the year at which the maximum amplitude (A) of the fitted sine function is reached. Note that locations with surficial dust/crust boundary are characterized by higher R^2 values (>0.7) in the sine fitting, also having a higher amplitude (A > 0.5) compared to sites without surficial dust/crust boundary.

Name	VH			VV			Dust & Crust?
	A (dB)	B_{MAXDOY}	R^{2*}	A (dB)	B_{MAXDOY}	R^{2*}	
Sediment Profile 10	1.78	256	0.84	1.08	257	0.89	yes
Surface Photo 1	1.68	252	0.80	1.19	254	0.87	yes
Surface Photo 2	1.38	256	0.77	0.98	251	0.84	yes
Surface Photo 6	1.15	267	0.75	0.66	262	0.82	yes
Sediment Profile 14	1.35	273	0.70	0.78	267	0.77	yes
Sediment Profile 13	1.25	242	0.69	0.78	242	0.76	yes
Sediment Profile 12	0.89	252	0.70	0.58	248	0.74	yes
Surface Photo 15	1.00	254	0.66	0.64	255	0.73	yes
Surface Photo 12	0.35	266	0.26	0.23	241	0.56	no
Sediment Profile 7	0.33	209	0.21	0.21	216	0.30	no
Sediment Profile 3	0.61	242	0.43	0.26	207	0.30	no
Sediment Profile 5	0.51	231	0.55	0.21	192	0.27	no
Sediment Profile 2	0.55	291	0.45	0.26	287	0.27	no
Surface Photo 9	0.15	238	0.20	0.07	242	0.18	no
Surface Photo 16	0.42	348	0.31	0.16	321	0.17	no
Surface Photo 5	0.32	239	0.07	0.22	259	0.12	no
Sediment Profile 6	0.37	294	0.23	0.11	258	0.11	no
Sediment Profile 11	0.26	110	0.06	0.37	160	0.11	no
Sediment Profile 1	0.15	213	0.12	0.08	255	0.09	no
Surface Photo 10	0.24	229	0.33	0.06	227	0.05	no
* R^2=	*< 0.25*	*< 0.50*	*< 0.70*	*< 0.8*	*< 1.0*		

be responsible for the observed SAR signal variations, ultimately caused by a moisture-regulated complex interplay of surface and subsurface scattering.

This interpretation is further supported by the observed difference between the VV and VH intensity. The VH-VV (dB) ratio was negatively correlated with the soil moisture content over the above-mentioned sites, therefore, VV and VH react differently to the changes in moisture. Comparing the scatterplots of VV, VH and VH-VV (Fig. 3 a-c) a stronger response of VH is observed with increasing moisture, which is in line with findings of Morrison and Wagner (2020) that indicate a higher dynamic range of the cross-pol. response compared to the co-pol. response. Taking this further, during wetting the VH response from the subsurface feature weakens, as the increased soil moisture will increase the attenuation in the upper layer. Depending on the roughness of the subsurface feature (i.e., here the indurated salt crust), the dynamic range of VH will be higher than the dynamic range of VV and, finally, the dynamic of the VH-VV ratio (i.e., lowering with wetting) can likely be explained by a stronger decrease with increasing moisture in VH relative to VV.

While it can be assumed that subsurface scattering effects can happen over very dry soils in general, the special setting in the uplands of the Coastal Cordillera of the Atacama Desert amplifies the effect of the inversion. This is followed by the strong changes in SAR backscatter (up to 5.5 dB in VH and up to 4.0 dB in VV) that was observed for remarkably small changes in soil moisture (ranging from approx. 1 to 3%) (ref. Table 2). As such extremely high absolute values (approx. 2 dB per 1%, on average) were observed. Similar high changes in SAR intensity from subsurface scattering effects (approx. 1 dB per 1%), were reported from laboratory experiments (Morrison, 2013). Besides the negative relation between SAR intensity and soil moisture, these values are much higher than values reported in literature for a positive relation between C-Band SAR intensity and soil moisture (approx. 0.12 dB per 1% for both VV and VH (El Hajj et al., 2018)), therefore it is unlikely that these strong variations can exclusively be explained by changing moisture content.

Our results also infer that the usage of SAR data to track such subtle seasonal changes in soil moisture in hyper-arid environments is restricted to sites, where the sedimentological setting facilitates subsurface scattering, as such as the setting magnifies the effect and the resulting changes in backscatter. Necessarily, a subsurface feature (i.e., here the crust) causing backscatter intensity well above the NESZ (Noise Equivalent Sigma Zero) is needed in dry state for the detection. The subtle changes in moisture would otherwise not be detectable by the C-Band SAR intensities of Sentinel-1, as a further decrease of intensity during wetting would cause intensities below the NESZ. Note in this context that VH intensities of Cerros de Calate go done to approx. -24 dB and might indicate the limit of detection close to the NESZ. Further, this also means that there is a critical penetration depth that is needed to cause a reflection at the crust surface, if the penetration of the microwaves is not reaching the dust/crust boundary the effect will not be observable. Besides constrains that arise from the NESZ it is worth noting that observed SAR signal variations (e.g., visible in Fig. 3 and Fig. A1) are close, or even below, the absolute radiometric accuracy that is reported in recent literature (e.g. El Hajj et al., 2016; Schmidt et al., 2020) with values ranging from 0.3 to 1.0 dB for VV intensity. To our interpretation, we can see a more accurate relative accuracy over the investigated locations, as the signal changes over time reveal a distinct non-random pattern. Additionally, it should be considered that for the presented stations we observe a VV span >2 dB, which means that the range between lowest and highest intensity is exceeding the absolute radiometric accuracy, same is true for VH span which is >4 dB (Table 2).

Besides, results indicate that the uplands of the Coastal Cordillera (characterized by a thick salt-rich layer of atmospheric dust (*chuka*) and buried cemented crust (*costra*)) do not exclusively provide a sedimentological setting facilitating and amplifying effects related to varying soil moisture. It was also observed that a strong linear correlation of SAR backscatter and soil moisture is present over regions towards the station Quebrada de Aroma. This leaves the possibility that other sedimentological settings may cause a similar magnitude of amplification; however, available reference data does yet not allow studying these effects in detail and, thus, these sites will be targeted in future research.

In this regard, also the complex behavior of some of the locations will be studied in detail to investigate the interplay of surface and subsurface scattering, also in the context of precipitation-based SM changes. These are revealed, for example, for the station Quebrada de Soga (Fig. 3). The locality experienced two strong rainfall events during the observation period (2019 and 2020) and these events caused a high increase in SM up to 50%. The S-1 observations show a complex response to these varying rain-induced SM conditions and no clear

(distinct) single pattern/behavior can be observed. Additionally, VV and VH seem to react at different sensitivity to SM changes once a certain wetness is reached. Exemplary, for VV the increase in intensity is particularly strong for SM > 30%, compared to VH. Due to this the response-pattern of VV is more "V-shaped" compared to the patterns of VH and VH-VV ratio.

4.2. Seasonal variations of near-surface soil moisture and SAR intensity

Taking the result on the inverse relationship between SAR intensity and near-surface soil moisture further, we studied the seasonal characteristics and spatial patterns of SAR intensities. This was done by fitting a sine function to the SAR time series. This function allows capturing and displaying the seasonal fluctuations of the SAR intensities. Introducing a minimum goodness of fit ($R^2 > 0.6$), and a minimum Amplitude (A) of the sine function (A > 0.5 dB), two distinct modes, shifted by 180 days, become visible/reveal across the area. These modes are exemplary highlighted in Fig. 8 by a boxplot series of a random sample, which was stratified by B_{MAXDOY}. The first mode (Fig. 8 a&b) displays variations with B_{MAXDOY} values between 210 and 290, while the second mode (Fig. 8 c&d) displays B_{MAXDOY} values between 30 and 110. The shapes of the two modes underline the phase shift, while the first mode exhibits the "inverse" situation (i.e., SAR intensities decreasing with increasing soil moisture), the second mode exemplifies the "normal" situation (i.e., SAR intensities increasing with increasing soil moisture), as the peaks of the second mode (Fig. 8 c&d) correspond well with the observed maximum soil moisture content across the in situ loggers (cf. Fig. 2). Note in this context that the applied sine fitting also indicated seasonal signal variations over the Salar Grande (Fig. 6 a&b), but with different B_{MAXDOY} values compared to sites in the central desert. These harmonic variations over the salar might be explained by changes in surface roughness due to weather conditions and salt crust formation (Delsouc et al., 2020).

At the same time, a striking spatial agreement with the presence of the anomaly and the geomorphological/environmental setting was observed (Fig. 6; Table 3). Strongest and most meaningful expression of the phenomena were nearly exclusively found over the central upland of the Coastal Cordillera (i.e., the hyper-arid core of the desert) that is characterized by the above-mentioned subsurface stratigraphy. This spatial agreement calls for the sedimentological setting to be responsible for the anomaly, especially when considering the seasonal fluctuations visible in both, the SAR and the in situ data record. The boundary to the west is demarked by the 1000 m contour line; thus, the occurrence of the effect seems to be caused/confined also by the occurrence of fog. Regions below the 1000 m contour were indicated by rather low R^2 (<0.6) of the sine fitting (Fig. 6 c&d) and a reason for this observation might be the more frequent appearance of the fog below this elevation. This is potentially causing a higher temporal variance of soil moisture changes and thus does not facilitate a clear regular oscillation belonging to specific seasons. Nevertheless, subsurface scattering may be present here but is not detectable by employing the sine fitting. To the east the anomaly is demarked by the boundary between the Coastal Cordillera and the Central Depression, this transition is characterized by a system of smaller alluvial fans and different surficial sediments without the

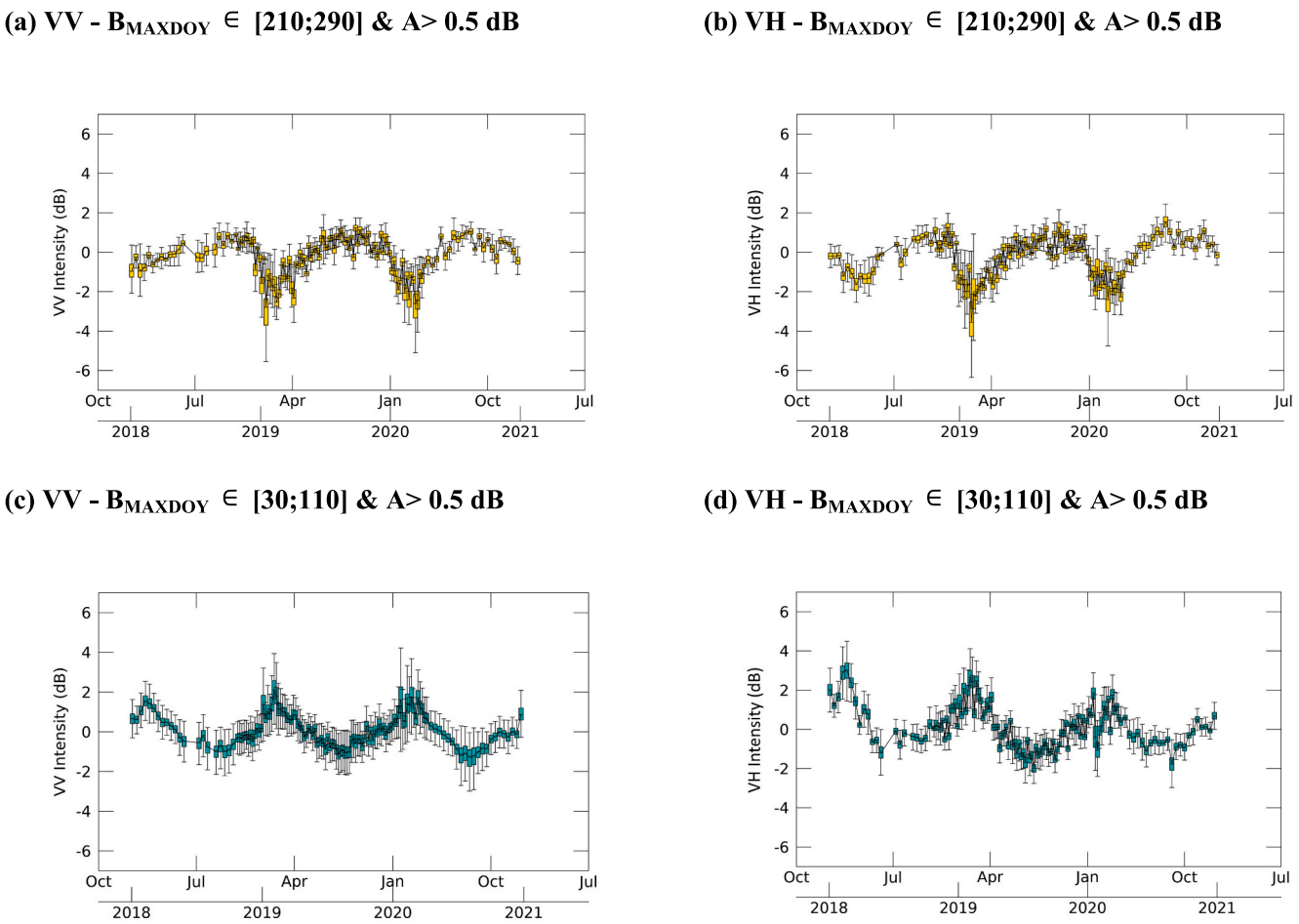

Fig. 8. Time series statistics (boxplots) of VV and VH estimated from a random sample ($n = 3000$) taken from areas with a Coefficient of Determination (R^2) higher 0.6, with a maximum amplitude A> 0.5 dB (see Fig. 6) and with (a-b) B_{MAXDOY} (day of the year at which A is reached) between 210 and 290, (c-d) B_{MAXDOY} between 30 and 110.

presence of thick dust deposits at the surface. It is characterized by an abrupt change from mountainous terrain with slopes towards flat alluvial plain and the distal alluvial fans of the Precordillera and/or with salar type strata.

4.3. Potential to map sites prone to subsurface scattering effects

Morrison and Wagner (2020) stated that analyzing the diversity in polarization and incidence angle might provide observations to flag regions prone to subsurface scattering, potentially also from the Sentinel-1 record. As indicated in this research, the different behavior of VV and VH and the inverse seasonal oscillation provided means to indicate localities where surface-scattering effects most likely occur. That was exemplified by strongly negative relations between the SAR intensities and the in situ measured soil moisture and might further extended using data acquired at different look angles (i.e., from different orbits). Nevertheless, this issue needs further elaboration, as also other sites (most likely not characterized by dust deposits and cemented crusts) were indicated by strong inverse seasonal fluctuations, as such other sedimentological/environmental factors need to be considered and researched, as also outlined by related studies (Bürgi and Lohman, 2021; Jordan et al., 2020; Scott et al., 2017). Further, it needs to be considered that differences in the inverse relation will be present as SAR intensities variations will be controlled first order by (i) the attenuation properties of the first layer and (ii) the roughness and composition of the second (buried) layer, thus not only by varying soil moisture content. For sites in the hyper-arid core of the Atacama this might be researched by investigating the composition of the dust deposits and the micromorphology of the cemented crusts (i.e., besides moisture, permittivity, roughness, and homogeneity of the individual soil layers). Sampling this information would support the generation of scattering models that can create a sound physical basis for the observed phenomenon and for SAR observations (Morrison and Wagner, 2020). These future efforts should be complemented by other concepts that were presented to analyze soil moisture variations in (hyper-)arid environments. For the Atacama Desert the studies on the interferometric coherence of Sentinel-1 have demonstrated that the InSAR coherence is sensitive to changing soil moisture (Jordan et al., 2020) and precipitation events (Scott et al., 2017; Ullmann et al., 2019). Similar, Bürgi and Lohmann (2021) have researched the InSAR coherence loss using Sentinel-1 time series related to changing soil moisture for arid study areas in Southern Arabian Peninsula.

5. Conclusions

This study investigates the relation between C-Band SAR backscatter and near-surface soil moisture (SM) in the hyper-arid environment of the Atacama Desert (Chile). Time series (2018–2020) of Sentinel-1 VV/VH intensities are compared to in situ SM, measured at several stations located across the Atacama Desert. Linear and non-linear regression modelling (using sine functions) is applied to uncover the relationship between the SAR intensities and in situ SM. Results indicate a very weak linear relationship between SM variations and SAR intensities (VV/VH) for most stations in the Atacama ($R^2 < 0.5$), while noticeable and significant exceptions are found for stations located in the northern uplands of the Coastal Cordillera and on sediments, which are characterized by thick atmospheric dust deposits on top of subsurface cemented crusts (confirmed for selected locations by sediment profiles). Over these sites a strong negative linear relationship is present (R^2 up to 0.84) and the observable seasonal variations in SAR intensity are linked to the seasonal variations in SM. Remarkably low changes in SM (around 2.5%) can lead to comparable high changes in SAR intensity (up to 5 dB), leading to high absolute values of change (approx. 2 dB per 1% on average). The reason for this strong inverse relationship is interpreted to be caused by subsurface scattering effects; a moisture-regulated complex interplay of surface and subsurface scattering.

Chances to use C-Band intensities of Sentinel-1 to estimate the near-surface soil moisture content in the hyper-arid environment of the Atacama Desert are nevertheless challenging. This is due to the presence of subsurface scattering effects that cause an inverse and/or complex relation between SAR intensity and soil moisture, also at sites not exhibiting the above-mentioned seasonal variations. Consequently, any area-wide modelling using SAR data would need to incorporate information on the properties of the surficial soil/sediment conditions at sufficient high spatial resolution to investigate these effects and needs to consider effects caused by different polarizations and/or acquisitions geometries. Further efforts using Sentinel-1 time series might take use of different look angles to identify regions that are prone to subsurface scattering and that exhibit an inverse relation between intensity and soil moisture. Concepts relying on the SAR phase alterations (Jordan et al., 2020; Morrison and Wagner, 2022) might be promising here in addition. Future research should also address modelling the influence of changing attention and roughness on the SAR intensities, this will allow approaching the identification of the critical penetration depth of the SAR signal and potentially the estimation of the thickness of the dust deposits in this hyper-arid environment.

Author contributions

Conceptualization, TU and SSM; data curation, TU, SSM, DH; formal analysis, all authors; funding acquisition, OB; investigation, all authors; methodology, TU; project administraion, OB, RB; resources, all authors; software, TU; supervision, OB, RB; writing—original draft preparation, TU; writing—review and editing, all authors; validation, all authors; visualization, TU and SSM. All authors have read and agreed to the published version of the manuscript.

Funding

This research was funded by the German Research Foundation (*Deutsche Forschungsgemeinschaft* DFG), within the project "CRC 1211: Earth - Evolution at the Dry Limit", grant number 268236062.

Declaration of Competing Interest

The authors declare that they have no known competing financial interests or personal relationships that could have appeared to influence the work reported in this paper.

Data availability

GLO-90 data (Copernicus Global Digital Elevation Model) is freely available through the European Space Agency (ESA) and was accessed via the Sentinel Application Platform (SNAP) Version 8 (*https://step.esa.int/main/toolboxes/snap*). Sentinel-1 is freely available, e.g., via the Copernicus Access Hub. GRD data of Sentinel-1 is freely accessible via the Google Earth Engine (*https://developers.google.com/earth-engine/datasets/catalog/COPERNICUS_S1_GRD*).

Acknowledgments

We thank the European Space Agency (ESA) for making Sentinel-1 data freely available to public. T.U. sincerely thanks Prof. Dr. Keith Morrison (University of Reading, United Kingdom) for his detailed explanation of his modelling results and the helpful discussion on the interpretation of subsurface scattering effects. We further thank Ms. Elly Schmid for the data curation. All authors thank the four anonymous reviewers for their valuable comments and suggestions.

Appendix A. Appendix

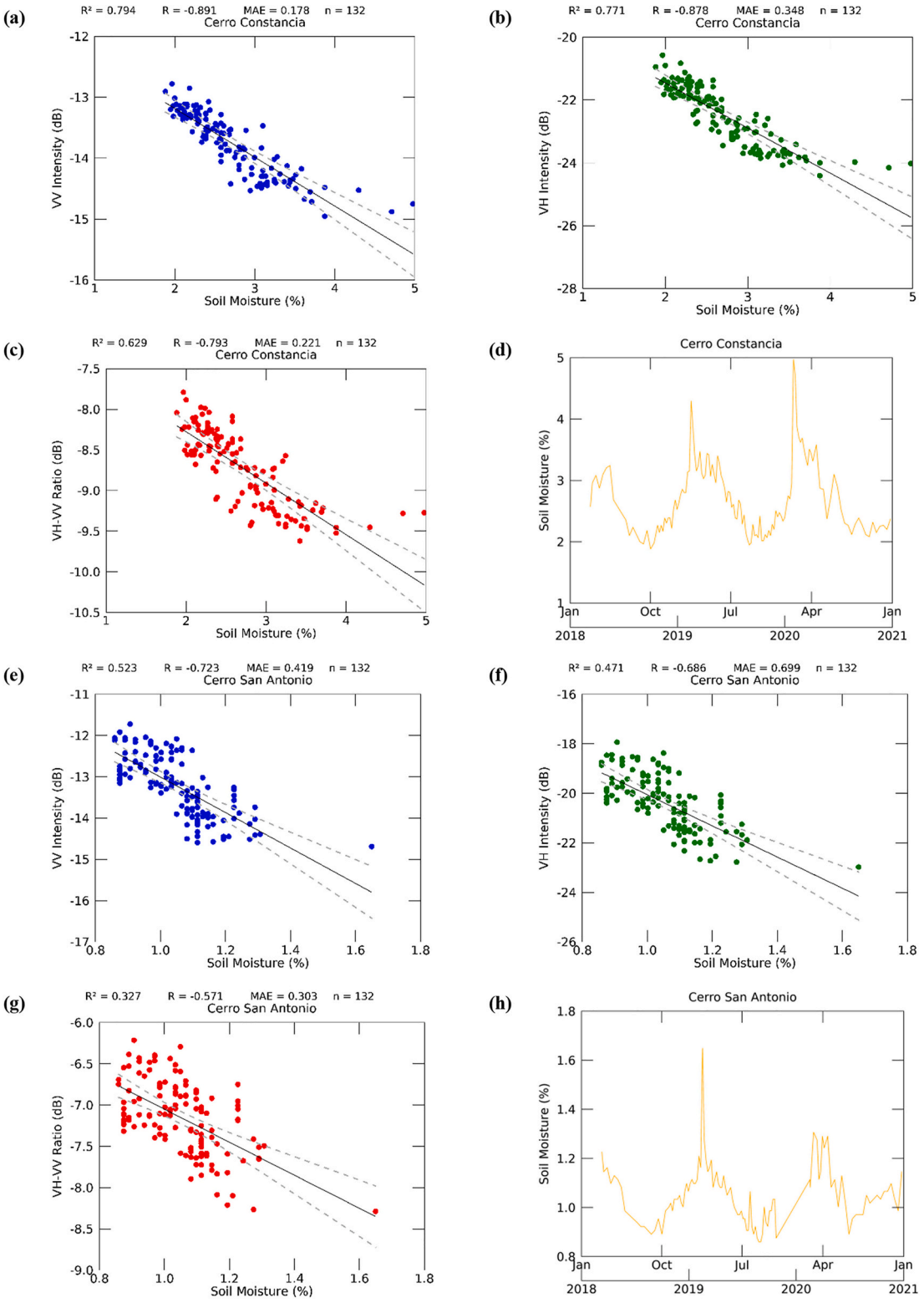

Fig. A1. Correlation between Sentinel-1 time series and near-surface soil moisture for the meteorological stations Cerro Constancia (a-d) and Cerro San Antonio (e-h): (a&e) soil moisture (%) vs. VV intensity (dB), (b&f) soil moisture (%) vs. VH intensity (dB), (c&g) soil moisture (%) vs. VV-VH intensity (dB), and (d&h) time series of the soil moisture (%). Grey dashed lines draw the lower and upper limit of the 95% confidence interval of linear regression. See Fig. 3 for further details.

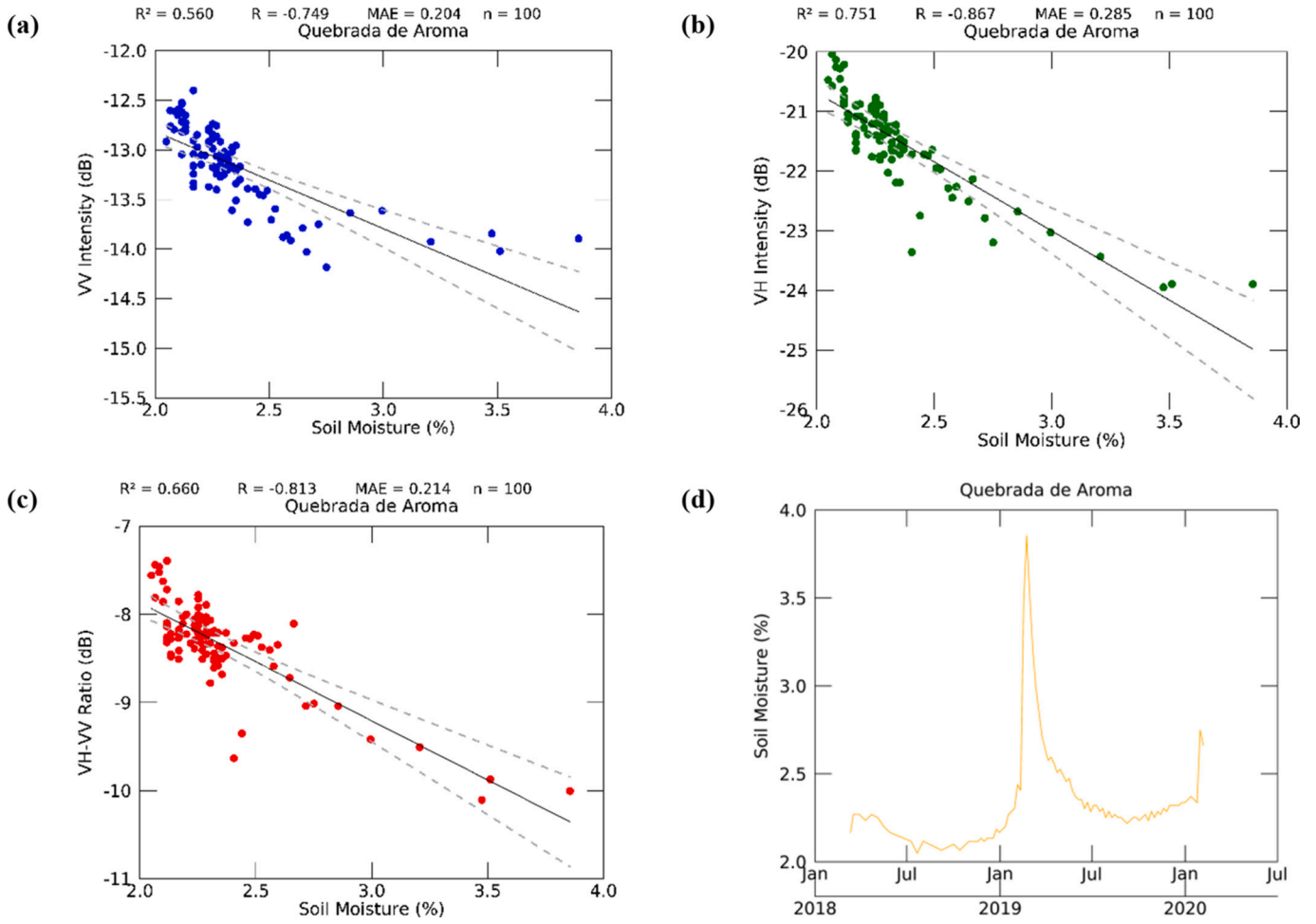

Fig. A2. Correlation between Sentinel-1 time series and near-surface soil moisture for the meteorological station Quebrada de Aroma: (a) soil moisture (%) vs. VV intensity (dB), (b) soil moisture (%) vs. VH intensity (dB), (c) soil moisture (%) vs. VV-VH intensity (dB), and (d) time series of the soil moisture (%). Grey dashed lines draw the lower and upper limit of the 95% confidence interval of linear regression. See Fig. 3 for further details.

References

Abele, G., 1990. Salzkrusten, salzbedingte solifluktion und steinsalzkarst in der nordchilenisch- peruanischen Wüste. Mainz. Geogr. Stud. 34, 23–46.

Arens, F.L., Airo, A., Feige, J., Sager, C., Wiechert, U., Schulze-Makuch, D., 2021. Geochemical proxies for water-soil interactions in the hyperarid Atacama Desert, Chile. CATENA 206, 105531. https://doi.org/10.1016/j.catena.2021.105531.

Balenzano, A., Mattia, F., Satalino, G., Lovergine, F.P., Palmisano, D., Peng, J., Marzahn, P., Wegmüller, U., Cartus, O., Dąbrowska-Zielińska, K., Musial, J.P., Davidson, M.W.J., Pauwels, V.R.N., Cosh, M.H., McNairn, H., Johnson, J.T., Walker, J.P., Yueh, S.H., Entekhabi, D., Kerr, Y.H., Jackson, T.J., 2021. Sentinel-1 soil moisture at 1 km resolution: a validation study. Remote Sens. Environ. 263, 112554 https://doi.org/10.1016/j.rse.2021.112554.

Barrett, B., Dwyer, E., Whelan, P., 2009. Soil moisture retrieval from active spaceborne microwave observations: an evaluation of current techniques. Remote Sens. 1, 210–242. https://doi.org/10.3390/rs1030210.

Bauer-Marschallinger, B., Freeman, V., Cao, S., Paulik, C., Schaufler, S., Stachl, T., Modanesi, S., Massari, C., Ciabatta, L., Brocca, L., Wagner, W., 2019. Toward global soil moisture monitoring with Sentinel-1: harnessing assets and overcoming obstacles. IEEE Trans. Geosci. Remote Sens. 57, 520–539. https://doi.org/10.1109/TGRS.2018.2858004.

Böhm, C., Reyers, M., Schween, J.H., Crewell, S., 2020. Water vapor variability in the Atacama Desert during the 20th century. Glob. Planet. Chang. 190, 103192 https://doi.org/10.1016/j.gloplacha.2020.103192.

Bojinski, S., Verstraete, M., Peterson, T.C., Richter, C., Simmons, A., Zemp, M., 2014. The concept of essential climate variables in support of climate research, applications, and policy. Bull. Am. Meteorol. Soc. 95, 1431–1443. https://doi.org/10.1175/BAMS-D-13-00047.1.

Bürgi, P.M., Lohman, R.B., 2021. High-resolution soil moisture evolution in hyper-arid regions: a comparison of InSAR, SAR, microwave, optical, and data assimilation Systems in the Southern Arabian Peninsula. JGR Earth Surf. 126 https://doi.org/10.1029/2021JF006158.

Cereceda, P., Osses, P., Larrain, H., Lagos, M., Pinto, R., Schemenauer, R.S., 2002. Advective, orographic and radiation fog in the Tarapacá region, Chile. In: Atmospheric Research, 2nd International Conference on Fog and Fog Collection, 64, pp. 261–271. https://doi.org/10.1016/S0169-8095(02)00097-2.

Chan, S.K., Bindlish, R., O'Neill, P.E., Njoku, E., Jackson, T., Colliander, A., Chen, F., Burgin, M., Dunbar, S., Piepmeier, J., Yueh, S., Entekhabi, D., Cosh, M.H., Caldwell, T., Walker, J., Wu, X., Berg, A., Rowlandson, T., Pacheco, A., McNairn, H., Thibeault, M., Martinez-Fernandez, J., Gonzalez-Zamora, A., Seyfried, M., Bosch, D., Starks, P., Goodrich, D., Prueger, J., Palecki, M., Small, E.E., Zreda, M., Calvet, J.-C., Crow, W.T., Kerr, Y., 2016. Assessment of the SMAP passive soil moisture product. IEEE Trans. Geosci. Remote Sens. 54, 4994–5007. https://doi.org/10.1109/TGRS.2016.2561938.

Clarke, J.D.A., 2006. Antiquity of aridity in the chilean Atacama Desert. Geomorphology 73, 101–114. https://doi.org/10.1016/j.geomorph.2005.06.008.

Colliander, A., Jackson, T.J., Bindlish, R., Chan, S., Das, N., Kim, S.B., Cosh, M.H., Dunbar, R.S., Dang, L., Pashaian, L., Asanuma, J., Aida, K., Berg, A., Rowlandson, T., Bosch, D., Caldwell, T., Caylor, K., Jassar, H., Lopez-Baeza, E., Martínez-Fernández, J., González-Zamora, A., Livingston, S., McNairn, H., Pacheco, A., Moghaddam, M., Montzka, C., Notarnicola, C., Niedrist, G., Pellarin, T., Prueger, J., Pulliainen, J., Rautiainen, K., Ramos, J., Seyfried, M., Starks, P., Su, Z., Zeng, Y., van der Velde, R., Thibeault, M., Dorigo, W., Vreugdenhil, M., Walker, J.P., Wu, X., Monerris, A., O'Neill, P.E., Entekhabi, D., Njoku, E.G., Yueh, S., Goodrich, D., 2017. Validation of SMAP surface soil moisture products with core validation sites. Remote Sens. Environ. 191, 215–231. https://doi.org/10.1016/j.rse.2017.01.021.

Das, N.N., Entekhabi, D., Dunbar, R.S., Chaubell, M.J., Colliander, A., Yueh, S., Jagdhuber, T., Chen, F., Crow, W., O'Neill, P.E., Walker, J.P., Berg, A., Bosch, D.D., Caldwell, T., Cosh, M.H., Collins, C.H., Lopez-Baeza, E., Thibeault, M., 2019. The SMAP and copernicus sentinel 1A/B microwave active-passive high resolution surface soil moisture product. Remote Sens. Environ. 233, 111380 https://doi.org/10.1016/j.rse.2019.111380.

de Porras, M.E., Maldonado, A., De Pol-Holz, R., Latorre, C., Betancourt, J.L., 2017. Late quaternary environmental dynamics in the Atacama Desert reconstructed from

rodent midden pollen records. J. Quat. Sci. 32, 665–684. https://doi.org/10.1002/jqs.2980.
Delsouc, A., Barber, M., Gallaud, A., Grings, F., Vidal-Páez, P., Pérez-Martínez, W., Briceño-De-Urbaneja, I., 2020. Seasonality Analysis of Sentinel-1 and ALOS-2/PALSAR-2 Backscattered Power over Salar de Aguas Calientes Sur, Chile. Remote Sens. 12, 941. https://doi.org/10.3390/rs12060941.
Dorigo, W., Wagner, W., Albergel, C., Albrecht, F., Balsamo, G., Brocca, L., Chung, D., Ertl, M., Forkel, M., Gruber, A., Haas, E., Hamer, P.D., Hirschi, M., Ikonen, J., de Jeu, R., Kidd, R., Lahoz, W., Liu, Y.Y., Miralles, D., Mistelbauer, T., Nicolai-Shaw, N., Parinussa, R., Pratola, C., Reimer, C., van der Schalie, R., Seneviratne, S.I., Smolander, T., Lecomte, P., 2017. ESA CCI soil moisture for improved earth system understanding: state-of-the art and future directions. Remote Sens. Environ. 203, 185–215. https://doi.org/10.1016/j.rse.2017.07.001.
Dostálová, A., Doubková, M., Sabel, D., Bauer-Marschallinger, B., Wagner, W., 2014. Seven years of advanced synthetic aperture radar (ASAR) global monitoring (GM) of surface soil moisture over Africa. Remote Sens. 6, 7683–7707. https://doi.org/10.3390/rs6087683.
Dunai, T.J., López, G.A.G., Juez-Larré, J., 2005. Oligocene-miocene age of aridity in the Atacama Desert revealed by exposure dating of erosion-sensitive landforms. Geology 33, 321–324. https://doi.org/10.1130/G21184.1.
El Hajj, M., Baghdadi, N., Bazzi, H., Zribi, M., 2018. Penetration analysis of SAR signals in the C and L bands for wheat, maize, and grasslands. Remote Sens. 11, 31. https://doi.org/10.3390/rs11010031.
El Hajj, M., Baghdadi, N., Zribi, M., Angelliaume, S., 2016. Analysis of Sentinel-1 radiometric stability and quality for land surface applications. Remote Sens. 8, 406. https://doi.org/10.3390/rs8050406.
Ericksen, G.E., 1983. The chilean nitrate deposits: the origin of the chilean nitrate deposits, which contain a unique group of saline minerals, has provoked lively discussion for more than 100 years. Am. Sci. 71, 366–374.
Ewing, S.A., Sutter, B., Owen, J., Nishiizumi, K., Sharp, W., Cliff, S.S., Perry, K., Dietrich, W., McKay, C.P., Amundson, R., 2006. A threshold in soil formation at Earth's arid–hyperarid transition. Geochim. Cosmochim. Acta 70, 5293–5322. https://doi.org/10.1016/j.gca.2006.08.020.
Ezzahar, J., Ouaadi, N., Zribi, M., Elfarkh, J., Aouade, G., Khabba, S., Er-Raki, S., Chehbouni, A., Jarlan, L., 2019. Evaluation of backscattering models and support vector machine for the retrieval of bare soil moisture from Sentinel-1 data. Remote Sens. 12, 72. https://doi.org/10.3390/rs12010072.
Fluhrer, A., Jagdhuber, T., Akbar, R., O'Neill, P.E., Entekhabi, D., 2021. Simultaneous retrieval of surface roughness parameters for bare soils from combined active-passive microwave SMAP observations. IEEE Trans. Geosci. Remote Sens. 59, 8182–8194. https://doi.org/10.1109/TGRS.2020.3035204.
Fryberger, S., Goudie, A.S., 1981. Arid geomorphology. Progr. Phys. Geogr. Earth Environ. 5, 420–428. https://doi.org/10.1177/030913338100500305.
Gorelick, N., Hancher, M., Dixon, M., Ilyushchenko, S., Thau, D., Moore, R., 2017. Google earth engine: planetary-scale geospatial analysis for everyone. Remote Sens. Environ. Big Remotely Sensed Data 202, 18–27. https://doi.org/10.1016/j.rse.2017.06.031.
Hänsch, R., Jagdhuber, T., Fersch, B., 2021. Soil-permittivity estimation under grassland using machine-learning and polarimetric decomposition techniques. IEEE Trans. Geosci. Remote Sens. 59, 2877–2887. https://doi.org/10.1109/TGRS.2020.3010104.
Hartley, A.J., Chong, G., Houston, J., Mather, A.E., 2005. 150 million years of climatic stability: evidence from the Atacama Desert, northern Chile. J. Geol. Soc. Lond. 162, 421–424. https://doi.org/10.1144/0016-764904-071.
Hoffmeister, D., 2018. Meteorological and soil measurements of the permanent weather stations in the Atacama desert. Chile. https://doi.org/10.5880/CRC1211DB.1.
Houston, J., Hartley, A.J., 2003. The central andean west-slope rainshadow and its potential contribution to the origin of hyper-aridity in the Atacama Desert. Int. J. Climatol. 23, 1453–1464. https://doi.org/10.1002/joc.938.
Jagdhuber, T., Hajnsek, I., Papathanassiou, K.P., 2015. An iterative generalized hybrid decomposition for soil moisture retrieval under vegetation cover using fully polarimetric SAR. IEEE J. Sel. Top. Appl. Earth Obs. Remote Sens. 8, 3911–3922. https://doi.org/10.1109/JSTARS.2014.2371468.
Jordan, T.E., La, C.H., Godfrey, L.V., Colucci, S.J., Paul, J.F., 2018. Isotopic characteristics and paleoclimate implications of the extreme precipitation event of March 2015 in northern Chile. Andean Geol. 46, 1–31. https://doi.org/10.5027/andgeoV46n1-3087.
Jordan, T.E., Lohman, R.B., Tapia, L., Pfeiffer, M., Scott, C.P., Amundson, R., Godfrey, L., Riquelme, R., 2020. Surface materials and landforms as controls on InSAR permanent and transient responses to precipitation events in a hyperarid desert, Chile. Remote Sens. Environ. 237, 111544 https://doi.org/10.1016/j.rse.2019.111544.
Kerr, Y.H., Waldteufel, P., Richaume, P., Wigneron, J.P., Ferrazzoli, P., Mahmoodi, A., Al Bitar, A., Cabot, F., Gruhier, C., Juglea, S.E., Leroux, D., Mialon, A., Delwart, S., 2012. The SMOS soil moisture retrieval algorithm. IEEE Trans. Geosci. Remote Sens. 50, 1384–1403. https://doi.org/10.1109/TGRS.2012.2184548.
Kornelsen, K.C., Coulibaly, P., 2013. Advances in soil moisture retrieval from synthetic aperture radar and hydrological applications. J. Hydrol. 476, 460–489. https://doi.org/10.1016/j.jhydrol.2012.10.044.
Latorre, C., Santoro, C.M., Ugalde, P.C., Gayo, E.M., Osorio, D., Salas-Egaña, C., De Pol-Holz, R., Joly, D., Rech, J.A., 2013. Late pleistocene human occupation of the hyperarid core in the Atacama Desert, northern Chile. Quat. Sci. Rev. 77, 19–30. https://doi.org/10.1016/j.quascirev.2013.06.008.
Legates, D.R., Mahmood, R., Levia, D.F., DeLiberty, T.L., Quiring, S.M., Houser, C., Nelson, F.E., 2011. Soil moisture: a central and unifying theme in physical geography. Progr. Phys. Geogr. 35, 65–86. https://doi.org/10.1177/0309133310386514.
Li, Z.-L., Leng, P., Zhou, C., Chen, K.-S., Zhou, F.-C., Shang, G.-F., 2021. Soil moisture retrieval from remote sensing measurements: current knowledge and directions for the future. Earth Sci. Rev. 218, 103673 https://doi.org/10.1016/j.earscirev.2021.103673.
Lictevout, E., Gocht, M., 2018. Hydrometric network design in hyper-arid areas: example of Atacama Desert (North Chile). Hydrol. Res. 49, 1208–1220. https://doi.org/10.2166/nh.2017.004.
Markwardt, C., 2009. Non-linear least squares fitting in IDL with MPFIT. In: Bohlender, D.A., Durand, D., Dowler, P. (Eds.), Astronomical Data Analysis Software and Systems XVIII: proceedings of a workshop held at Hotel Loews Le Concorde, Quebec City, QC, Canada, 2-5 November 2008, Astronomical Society of the Pacific Conference Series. Presented at the Astronomical Data Analysis Software and Systems. Astronomical Society of the Pacific, San Francisco, Calif.
Matmon, A., Quade, J., Placzek, C., Fink, D., Arnold, M., Aumaître, G., Bourlès, D., Keddadouche, K., Copeland, A., Neilson, J.W., 2015. Seismic origin of the Atacama Desert boulder fields. Geomorphology 231, 28–39. https://doi.org/10.1016/j.geomorph.2014.11.008.
May, S.M., Hoffmeister, D., Ullmann, T., Bubenzer, O., 2020. Geomorphic processes and the stability of surfaces in the central Atacama Desert (Chile) - comparing Sentinel-1 InSAR coherence time series and field evidence. In: EGU General Assembly Conference Abstracts, EGU General Assembly Conference Abstracts, p. 19878.
May, S.M., Hoffmeister, D., Wolf, D., Bubenzer, O., 2019. Zebra stripes in the Atacama Desert revisited – granular fingering as a mechanism for zebra stripe formation? Geomorphology 344, 46–59. https://doi.org/10.1016/j.geomorph.2019.07.014.
Medialdea, A., May, S.M., Brill, D., King, G., Ritter, B., Wennrich, V., Bartz, M., Zander, A., Kuiper, K., Hurtado, S., Hoffmeister, D., Schulte, P., Gröbner, M., Opitz, S., Brückner, H., Bubenzer, O., 2020. Identification of humid periods in the Atacama Desert through hillslope activity established by infrared stimulated luminescence (IRSL) dating. Glob. Planet. Chang. 185, 103086 https://doi.org/10.1016/j.gloplacha.2019.103086.
Michalski, G., Böhlke, J.K., Thiemens, M., 2004. Long term atmospheric deposition as the source of nitrate and other salts in the Atacama Desert, Chile: new evidence from mass-independent oxygen isotopic compositions. Geochim. Cosmochim. Acta 68, 4023–4038. https://doi.org/10.1016/j.gca.2004.04.009.
Montzka, C., Bogena, H.R., Herbst, M., Cosh, M.H., Jagdhuber, T., Vereecken, H., 2021. Estimating the number of reference sites necessary for the validation of global soil moisture products. IEEE Geosci. Remote Sens. Lett. 18, 1530–1534. https://doi.org/10.1109/LGRS.2020.3005730.
Montzka, C., Jagdhuber, T., Horn, R., Bogena, H.R., Hajnsek, I., Reigber, A., Vereecken, H., 2016. Investigation of SMAP fusion algorithms with airborne active and passive L-band microwave remote sensing. IEEE Trans. Geosci. Remote Sens. 54, 3878–3889. https://doi.org/10.1109/TGRS.2016.2529659.
Morrison, K., 2013. Mapping subsurface archaeology with SAR: mapping subsurface archaeology with SAR. Archaeol. Prospect. 20, 149–160. https://doi.org/10.1002/arp.1445.
Morrison, K., Wagner, W., 2022. Soil moisture and soil depth retrieval using the coupled phase-amplitude behavior of C-band radar backscatter in the presence of sub-surface scattering. Can. J. Remote. Sens. 1–14 https://doi.org/10.1080/07038992.2022.2120858.
Morrison, K., Wagner, W., 2020. Explaining anomalies in SAR and scatterometer soil moisture retrievals from dry soils with subsurface scattering. IEEE Trans. Geosci. Remote Sens. 58, 2190–2197. https://doi.org/10.1109/TGRS.2019.2954771.
Owen, J.J., Dietrich, W.E., Nishiizumi, K., Chong, G., Amundson, R., 2013. Zebra stripes in the Atacama Desert: fossil evidence of overland flow. Geomorphology 182, 157–172. https://doi.org/10.1016/j.geomorph.2012.11.006.
Quade, J., Reiners, P., Placzek, C., Matmon, A., Pepper, M., Ojha, L., Murray, K., 2012. Seismicity and the strange rubbing boulders of the Atacama Desert, northern Chile. Geology 40, 851–854. https://doi.org/10.1130/G33162.1.
Rech, J.A., Quade, J., Hart, W.S., 2003. Isotopic evidence for the source of ca and S in soil gypsum, anhydrite and calcite in the Atacama Desert, Chile. Geochim. Cosmochim. Acta 67, 575–586. https://doi.org/10.1016/S0016-7037(02)01175-4.
Richards, J.A., 2009. Remote Sensing with Imaging Radar, Signals and Communication Technology. Springer Berlin Heidelberg, Berlin, Heidelberg. https://doi.org/10.1007/978-3-642-02020-9.
del Río, C.G., Rivera, D.S., Siegmund, A., Wolf, N., Cereceda, P., Larraín, H., Lobos, F., Garcia, J.L., Osses, P., Zanetta, N., Lambert, F., 2018. ENSO influence on coastal fog-water yield in the Atacama Desert. Chile. https://doi.org/10.4209/aaqr.2017.01.0022.
Rundel, P., Dillon, M., Palma, B., Mooney, H., Gulmon, S., Ehleringer, J., 1991. The phytogeography and ecology of the coastal Atacama and Peruvian deserts. Aliso 13, 1–49. https://doi.org/10.5642/aliso.19911301.02.
Sadeh, Y., Cohen, H., Maman, S., Blumberg, D., 2018. Evaluation of Manning's n roughness coefficient in arid environments by using SAR backscatter. Remote Sens. 10, 1505. https://doi.org/10.3390/rs10101505.
Sano, E.E., Huete, A.R., Troufleau, D., Moran, M.S., Vidal, A., 1998. Relation between ERS-1 synthetic aperture radar data and measurements of surface roughness and moisture content of rocky soils in a semiarid rangeland. Water Resour. Res. 34, 1491–1498. https://doi.org/10.1029/98WR00032.
Schmidt, K., Schwerdt, M., Miranda, N., Reimann, J., 2020. Radiometric comparison within the Sentinel-1 SAR constellation over a wide backscatter range. Remote Sens. 12, 854. https://doi.org/10.3390/rs12050854.
Schween, J.H., Hoffmeister, D., Löhnert, U., 2020. Filling the observational gap in the Atacama Desert with a new network of climate stations. Glob. Planet. Chang. 184, 103034 https://doi.org/10.1016/j.gloplacha.2019.103034.

Scott, C.P., Lohman, R.B., Jordan, T.E., 2017. InSAR constraints on soil moisture evolution after the march 2015 extreme precipitation event in Chile. Sci. Rep. 7, 4903. https://doi.org/10.1038/s41598-017-05123-4.

Seneviratne, S.I., Corti, T., Davin, E.L., Hirschi, M., Jaeger, E.B., Lehner, I., Orlowsky, B., Teuling, A.J., 2010. Investigating soil moisture–climate interactions in a changing climate: a review. Earth Sci. Rev. 99, 125–161. https://doi.org/10.1016/j.earscirev.2010.02.004.

Shao, Y., Fraedrich, K., Ishizuka, M., 2021. Modelling soil moisture in hyper-arid conditions. Boundary-Layer Meteorol. 179, 169–186. https://doi.org/10.1007/s10546-020-00596-9.

Suman, S., Srivastava, P.K., Petropoulos, G.P., Pandey, D.K., O'Neill, P.E., 2020. Appraisal of SMAP operational soil moisture product from a global perspective. Remote Sens. 12, 1977. https://doi.org/10.3390/rs12121977.

Ulaby, F.T., Long, D.G., 2014. Microwave radar and radiometric remote sensing. The University of Michigan Press, Ann Arbor.

Ullmann, T., Sauerbrey, J., Hoffmeister, D., May, S.M., Baumhauer, R., Bubenzer, O., 2019. Assessing spatiotemporal variations of Sentinel-1 InSAR coherence at different time scales over the Atacama Desert (Chile) between 2015 and 2018. Remote Sens. 11, 2960. https://doi.org/10.3390/rs11242960.

Ullmann, T., Stauch, G., 2020. Surface roughness estimation in the orog Nuur Basin (Southern Mongolia) using Sentinel-1 SAR time series and ground-based photogrammetry. Remote Sens. 12, 3200. https://doi.org/10.3390/rs12193200.

Voigt, C., Klipsch, S., Herwartz, D., Chong, G., Staubwasser, M., 2020. The spatial distribution of soluble salts in the surface soil of the Atacama Desert and their relationship to hyperaridity. Glob. Planet. Chang. 184, 103077 https://doi.org/10.1016/j.gloplacha.2019.103077.

Wagner, W., Blöschl, G., Pampaloni, P., Calvet, J.-C., Bizzarri, B., Wigneron, J.-P., Kerr, Y., 2007. Operational readiness of microwave remote sensing of soil moisture for hydrologic applications. Hydrol. Res. 38, 1–20. https://doi.org/10.2166/nh.2007.029.

Wagner, W., Hahn, S., Kidd, R., Melzer, T., Bartalis, Z., Hasenauer, S., Figa-Saldaña, J., de Rosnay, P., Jann, A., Schneider, S., Komma, J., Kubu, G., Brugger, K., Aubrecht, C., Züger, J., Gangkofner, U., Kienberger, S., Brocca, L., Wang, Y., Blöschl, G., Eitzinger, J., Steinnocher, K., 2013. In: The ASCAT Soil Moisture Product: A Review of its Specifications, Validation Results, and Emerging Applications, 22. metz, pp. 5–33. https://doi.org/10.1127/0941-2948/2013/0399.

Wagner, W., Lindorfer, R., Melzer, T., Hahn, S., Bauer-Marschallinger, B., Morrison, K., Calvet, J.-C., Hobbs, S., Quast, R., Greimeister-Pfeil, I., Vreugdenhil, M., 2022. Widespread occurrence of anomalous C-band backscatter signals in arid environments caused by subsurface scattering. Remote Sens. Environ. 276, 113025 https://doi.org/10.1016/j.rse.2022.113025.

Wang, F., Michalski, G., Luo, H., Caffee, M., 2017. Role of biological soil crusts in affecting soil evolution and salt geochemistry in hyper-arid Atacama Desert, Chile. Geoderma 307, 54–64. https://doi.org/10.1016/j.geoderma.2017.07.035.

Wang, L., Qu, J.J., 2009. Satellite remote sensing applications for surface soil moisture monitoring: a review. Front. Earth Sci. China 3, 237–247. https://doi.org/10.1007/s11707-009-0023-7.

Wilcox, A.C., Escauriaza, C., Agredano, R., Mignot, E., Zuazo, V., Otárola, S., Castro, L., Gironás, J., Cienfuegos, R., Mao, L., 2016. An integrated analysis of the march 2015 Atacama floods. Geophys. Res. Lett. 8035–8043 https://doi.org/10.1002/2016GL069751.

Yang, L., Feng, X., Liu, F., Liu, J., Sun, X., 2019. Potential of soil moisture estimation using C-band polarimetric SAR data in arid regions. Int. J. Remote Sens. 40, 2138–2150. https://doi.org/10.1080/01431161.2018.1516320.

Yang, L., Sun, G., Zhi, L., Zhao, J., 2018. Negative soil moisture-precipitation feedback in dry and wet regions. Sci. Rep. 8, 4026. https://doi.org/10.1038/s41598-018-22394-7.